Earthquake Engineering & Structural Dynamics

WILEY

RESEARCH ARTICLE OPEN ACCESS

Displacement Estimation of Structures With Flag-Shaped Hysteresis Loops

Yudi Zhang[1] | Gregory A. MacRae[1] | Geoffrey W. Rodgers[2] | Shahab Ramhormozian[3] | Charles Clifton[4] | Masoumeh Farshbaf[5]

[1]Civil and Environmental Engineering, University of Canterbury, Christchurch, New Zealand | [2]Mechanical Engineering, University of Canterbury, Christchurch, New Zealand | [3]School of Future Environments, Auckland University of Technology, Auckland, New Zealand | [4]Civil and Environmental Engineering, University of Auckland, Auckland, New Zealand | [5]Department of Structural Engineering, International Institute of Earthquake Engineering and Seismology (IIEES), Tehran, Iran

Correspondence: Yudi Zhang (yudi.zhang@pg.canterbury.ac.nz)

Received: 28 May 2026 | **Revised:** 3 September 2026 | **Accepted:** 4 September 2026

Keywords: cumulative displacement | deformation cycles | displacement prediction | period-duration ratio | rocking structure | tension-only frictional dissipator

ABSTRACT

Time-history analyses were conducted on single-degree-of-freedom (SDOF) systems with flag-shaped hysteresis loops using a far-field ground motion suite to estimate peak displacements, Δ_p, and equivalent deformation cycles, N_c, associated with cumulative displacement demands. The varied parameters included loop dissipation parameters β (0.1 to 1), strength-reduction factors R (2 to 8), positive post-yield stiffness ratios r (0 to 0.9), structural periods T (0.2 s to 3.5 s), period-to-earthquake-record-duration ratios T/D (0.014 to 0.25), and viscous damping models. Empirical equations were proposed for the mean Δ_p and N_c. A comparison was made with responses of a three-storey rocking structure with tension-only friction dissipators (TOFDs). Using T/D instead of T improved displacement predictability for short-period structures and gave similar accuracy for longer-period structures. The greatest Δ_p occurred in low-dissipation structures with $\beta = 0.1$, $r = 0.0$, $R = 8$, and $T/D = 0.014$. Conventional displacement estimation methods may underpredict Δ_p. The largest N_c occurred for $r = 0.9$, $\beta = 0.1$, $R = 8$, and $T/D = 0.014$. Conservative equations were proposed for Δ_p considering β, R, and T/D with $r = 0.0$, giving a coefficient of determination R^2 of 0.89. For N_c, using $r = 0.3$ as a practical upper-bound representative of common structures, conservative equations were proposed with R^2 of 0.91. The mean Δ_p and cumulative TOFD displacement of the rocking structure subjected to the ground motion suite were similar to those from SDOF systems with matching β, R, r, and T. The empirical equations provided conservative predictions for the rocking-structure responses.

1 | Introduction

Structures with fat hysteresis loops, representing steel moment frame structures or non-buckling braced structures with buckling-restrained braces (BRBs) or friction braces, are commonly used in seismic regions. Some structures have moderately pinched hysteresis loops, such as many reinforced concrete structures. Others can have very pinched loops, such as timber structures or rocking structures designed specifically for self-centering. For structures with fat and moderately pinched hysteresis loops, methods commonly used to predict displacements are generally based on the initial stiffness, and the calibrations were initially conducted using initial stiffness proportional damping models. For structures with more pinched hysteresis loops, there may be greater responses and secant-stiffness-based methods, which consider the unloading part of the hysteresis curve, are sometimes preferred. However, neither of these approaches explicitly accounts for record duration, which can influence displacement demands. Furthermore, the number of deformation cycles used to test structural components in standard test protocols is specified independently of the hysteresis loop shape, while it could be expected that longer duration records will result in more deformation cycles.

There is a need for a unified approach to estimate peak displacements, Δ_p, so that engineers have confidence in the design of structures with a wide range of hysteresis loop shapes explicitly considering the earthquake record duration, D. Similarly, a method for estimating the number of cycles of deformation, N_c, is required for structural test regimes.

This paper takes a step in addressing the needs above using single-degree-of-freedom (SDOF) structures by seeking answers to the following questions:

1. What methods have been proposed in previous studies to estimate the peak displacements and number of deformation cycles of simple structures during earthquake shaking, and what are their key characteristics and limitations?
2. How does tangent-stiffness proportional damping affect the peak displacements and number of deformation cycles?
3. How do various structural parameters affect the peak displacements, Δ_p?
4. How do various structural parameters influence the number of deformation cycles, N_c?
5. What gives a better prediction of response, structural period, T, or period-to-duration ratio, T/D?
6. Can empirical equations be developed to estimate the structural demands?
7. How can the findings above be applied to the design of a three-storey rocking structure?

2 | Previous Work

2.1 | Displacement Estimation

Commonly used approaches for estimating nonlinear seismic displacement demands can be broadly classified into two categories: initial-stiffness-based methods and secant-stiffness-based methods. These two methods are reviewed below.

2.1.1 | Initial-Stiffness-Based Methods

The initial-stiffness-based methods, which modify the displacement response of an equivalent elastic SDOF system with the same initial elastic stiffness, have been commonly used in standards around the world to estimate nonlinear structural displacements because of their simplicity. This philosophy originates from classical spectral-reduction concepts proposed by Newmark [1], where inelastic demands are approximated by scaled elastic spectra. For long-period structures, the initial-stiffness-based methods often rely on the equal-displacement principle, which assumes that the peak inelastic displacement is equal to the corresponding elastic displacement. This assumption does not always hold for short-period structures and modification is needed to obtain nonlinear displacement demands. The theoretical basis for inelastic displacement demands exceeding the corresponding elastic displacement demands, particularly in short-period structures, can be traced to Housner [2]. An important energy-based perspective was provided in this study by relating structural responses to the energy input from earthquakes and the corresponding energy dissipation through inelastic deformation, which later became closely associated with the equal-energy concept. Building on this research, Newmark and Hall [3] further idealized seismic response in terms of characteristic spectral regions, commonly linked to equal-acceleration, equal-energy, and equal-displacement concepts over short-, intermediate-, and long-period ranges. Berrill et al. [4] proposed a relationship based on these concepts, which was subsequently adopted in bridge seismic design (NZNSEE Bridge Study Group [5]) and later incorporated into structural seismic design (NZS 4203 [6]) in New Zealand and then others internationally. Representative initial-stiffness-based methods include the following.

1. FEMA 356 [7]

FEMA 356 [7] estimated the peak nonlinear displacement Δ_p by modifying the elastic displacement Δ_e using the coefficients C_1 and C_2, as shown in Equation 1. Coefficient C_1 accounts for inelastic response amplification and is calculated using Equation 2 as a function of the strength-reduction factor R, the structure period T and the transition period T_s, following Berrill et al. [4]. The transition period T_s is defined as the characteristic period at which the response spectrum transitions from the constant-acceleration region to the constant-velocity region; therefore, it depends on the spectral parameters and is indirectly related to the site class. The coefficient C_2 was introduced to account for the effects of pinched hysteretic shapes, stiffness degradation, and strength deterioration. This treatment is consistent with the findings of Song and Pincheira [8], who showed that pinched and degrading hysteretic systems may exhibit amplified displacement demands relative to non-degrading systems. Its value is specified according to the period, framing type and structural performance level. The minimum value of C_2 is 1.0, while the maximum value is 1.5.

$$\Delta_p = C_1 \cdot C_2 \cdot \Delta_e \tag{1}$$

$$C_1 = [1 + (R - 1)\, T_S / T] / R \tag{2}$$

2. Miranda [9]

Miranda [9] showed that for structures on firm sites with average shear-wave velocities greater than 180 m/s, the influence of further site subclassification on the mean inelastic displacement ratio, C_μ, was within 10% and can be neglected for design purposes. The study also showed that the applicability of the equal-displacement rule depended on the level of the inelastic deformation. The limiting period beyond which this rule applied increased with increasing displacement ductility. Based on these findings, Miranda [9] then proposed a simplified expression for C_μ for all the firm sites, as expressed by Equation 3, where μ_M is the displacement ductility ratio. This expression did not require the estimation of a characteristic site period and provided a continuous empirical representation of the effects of both T and μ_M on inelastic displacement ratios without relying on a fixed transition period. Note that since $R = \Delta_e/\Delta_y$ and $C_\mu = \Delta_p/\Delta_e$, where

Δ_y is the yield displacement, it follows that $\mu_M = \Delta_p/\Delta_y = C_\mu R$. Accordingly, for a given R and T, Equation 3 can be used together with $\mu_M = C_\mu R$ to obtain the corresponding μ_M and C_μ through an iterative solution procedure.

$$C_\mu = 1 \Big/ \left[1 + (1/\mu_M - 1) \cdot \left(e^{-12T\mu_M^{-0.8}}\right)\right] \tag{3}$$

3. NZS1170.5 [10]

The nonlinear displacement, as shown in Equation 4, was expressed as the product of the yield displacement Δ_y and the displacement ductility ratio μ_N calculated by Equation 5. For site subsoil classes A–D, this expression is formally analogous to that of Berrill et al. [4], where NZS1170.5 [10] adopts a constant transition period of 0.7 s.

$$\Delta_p = \mu_N \cdot \Delta_y \tag{4}$$

$$\mu_N = 1 + (R - 1) \cdot 0.7s/T \tag{5}$$

4. SCNZ [11]

For rocking structures, SCNZ [11] applied a 1.3 amplification factor to the displacement estimated from Equation 4 to account for the effect of the pinched hysteretic loop shape, as illustrated in Equation 6. This gives a step change before and after Δ_y. Rangwani et al. [12] removed the step function based on a limited number of analyses.

$$\Delta_p = 1.3\mu_N \cdot \Delta_y \tag{6}$$

Earthquake duration effects are not considered explicitly in the equations above. These may be important as shown by MacRae [13], Chandramohan et al. [14], and Raghunandan and Liel [15]. Furthermore, Farshbaf et al. [16] have shown that displacement demands increase with a greater ratio of the earthquake duration to the structural period. This effect is particularly significant for very pinched hysteresis loops.

Erduran and Kunnath [17] note that although initial-stiffness-based methods were widely used in practice, they were primarily calibrated for conventional yielding structural systems and less work has been undertaken to estimate demands for structures with pinched hysteresis responses. Other studies on pinched loops include those by Christopoulos et al. [18], who numerically investigated the seismic response of flag-shaped SDOF systems, showing that these systems can achieve the same or better response than elastic-perfectly plastic systems, and residual displacements can be zero. Christopoulos [19] further examined their nonlinear frequency-response characteristics, developing closed-form equations to characterize different types of behaviour. Kitayama and Constantinou [20–22] conducted analyses of SDOF systems with fluidic self-centring systems and established practical guidance for selecting self-centring device properties in design.

2.1.2 | Secant-Stiffness-Based Methods

Secant-stiffness-based methods estimate inelastic displacement demands using an equivalent elastic SDOF system defined by the secant stiffness at the peak response, rather than the initial elastic stiffness.

1. Gulkan and Sozen [23]

The Gulkan and Sozen method approximated the inelastic structure response by the peak response of the equivalent SDOF system with the damping ratio $\zeta_{e,G}$ calculated by Equation 7, where ζ_0 represents the initial elastic damping, ζ_{hyst} is the hysteretic viscous damping, and E_d and E_s denote the area enclosed by the hysteretic loop and the strain energy at the peak displacement, respectively.

$$\zeta_{e,G} = \zeta_0 + \zeta_{hyst} = \zeta_0 + E_d/(4\pi E_s) \tag{7}$$

1. Priestley [24]

The Priestley method was proposed based on the Gulkan and Sozen method, but the calculation of effective damping ratios $\zeta_{e,P}$ is different, as expressed by Equation 8, where μ_p is the ductility ratio, $\mu_p^{-0.43}$ is the modification factor for elastic damping when a tangent-stiffness dependent viscous damping is adopted in the nonlinear analyses, and f_c is the correction factor for hysteretic damping, as defined by Equation 9.

$$\zeta_{e,P} = \mu_P^{-0.43}\zeta_0 + f_c\zeta_{hyst} \tag{8}$$

$$f_c = -1.8\zeta_{hyst} + (0.0875\mu_P + 0.723) \tag{9}$$

Although these methods better reflected the effective stiffness at peak responses and energy dissipation, they were calibrated based on a specific suite of earthquake records and still did not explicitly incorporate the influence of the ground-motion duration or cumulative cyclic demands. In addition, for flag-shaped or hybrid structural systems, the available equivalent-damping expressions show considerable scatter and require further calibration against nonlinear response-history analyses to achieve reliable displacement prediction (Ceballos and Sullivan [25], Sullivan [26], and Zhou et al. [27]). The lack of consistency of the secant stiffness methods can also be seen when considering a ground motion excitation which causes only one large monotonic pulse (as many earthquake records do). In this case, after the pulse there is very little excitation, so the unloading characteristics of the hysteretic behaviour, i.e., hysteretic viscous damping, are irrelevant to the peak response, while for a long excitation earthquake, the unloading characteristics are important. Other inadequacies of these methods have been shown by MacRae [28].

2.2 | Number of Cycles of Deformation

The inelastic performance of a structural member is dependent not only on peak displacements, but also on the number of cycles of deformation experienced during earthquake excitation. This concept has been recognized in earthquake engineering, particularly in studies on cumulative damage and low-cycle fatigue, where repeated inelastic excursions contribute progressively to structural degradation (e.g. Krawinkler and Zohrei [29], Park and Ang [30], and MacRae [31]). To characterize the cyclic effect more quantitatively, MacRae and Kawashima [32] and Hancock and Bommer [33] used the effective number of cycles N_c and Cook [34] and Du et al. [35] further proposed empirical prediction equations for the effective number of cycles.

One of the primary factors influencing the number of deformation cycles is ground-motion duration. Arias [36] introduced Arias intensity as a measure of the cumulative energy content of ground motions, which later formed the basis for the commonly used definition of the significant earthquake duration proposed by Trifunac and Brady [37] and Bommer and Martínez-Pereira [38]. Hancock and Bommer [33] and Bommer et al. [39] showed that the damaging potential of earthquake ground motions depended not only on shaking amplitude but also on the earthquake duration, and that longer-duration motions were generally associated with a greater number of cycles of deformation. In addition to ground-motion characteristics, the structural fundamental period has also been shown to play an important role in governing the number of deformation cycles. Studies on nonlinear SDOF systems indicated that short-period structures tended to experience a larger number of significant response cycles, whereas long-period structural systems were often dominated by fewer large-amplitude excursions (MacRae and Kawashima [32]). These aspects were not generally considered in loading protocols for structures (e.g. Park [40], and AISC [41]) and an underestimation of the number of cycles during an earthquake may lead to unanticipated poor performance. Furthermore, the shape of the hysteretic response also influenced cyclic demands. For SDOF systems subjected to earthquake loading, loop shapes with lower energy dissipation, including more pinched or flag-shaped responses, were found to be associated with larger effective numbers of deformation cycles (e.g. Farshbaf et al. [42]). Farshbaf et al. [16] indicated that rather than the period itself, the period-to-duration ratio, T/D, may be important in determining N_c for all structures, including for rocking systems equipped with tension-only friction dissipators (TOFDs) where cumulative tensile deformations of the friction connections occur as a result of ratcheting under repeated uplift cycles (Cook et al. [34], and Rangwani et al. [12]).

3 | Methodology

3.1 | SDOF Models

To investigate how hysteretic behaviour, earthquake intensity, damping, and shaking duration influence peak displacement and the number of deformation cycles during earthquake excitation, nonlinear time-history analyses were conducted on a series of idealized SDOF models. The SDOF models represent equivalent single-storey structural systems with various hysteretic loops. The structural mass, M, was assumed to remain constant for all models, while the fundamental period, T, was varied to represent different stiffness levels. For a specified period, the initial lateral stiffness, K, was determined from Equation 10. The lateral yield strength, F_y, was defined as a function of the elastic spectral acceleration, S_a, the strength-reduction factor, R, and the gravitational acceleration, g, as shown in Equation 11.

$$K = (2\pi/T)^2 M \tag{10}$$

$$F_y = (S_a M g)/R \tag{11}$$

Twenty-two pairs of far-field ground motion records with different shaking duration values were selected from FEMA P695 [43]. Because the SDOF systems were unidirectional, the two horizontal components of each record pair were treated as independent single-component acceleration records and were not applied simultaneously. Thus, the response database was generated using 44 unidirectional far-field acceleration records. To characterize the effective duration of strong shaking, the significant duration, D, of Trifunac and Brady [37] was calculated for each ground motion record. This parameter was defined as the time interval over which the cumulative Arias intensity increases from 5% to 95% of its final value. The selected ground motion dataset had an average significant duration of approximately 14 s. Each ground motion was scaled such that its spectral acceleration at a specified reference period matched the corresponding code-based design spectral acceleration (NZS 1170.5 [10]). The strength-reduction factors considered were R = 2, 4, 6, and 8. All nonlinear time-history analyses were performed using the OpenSees software (Mazzoni et al. [44]). Time integration was carried out using the Newmark constant-average-acceleration method. To assess the sensitivity of the analytical results to viscous damping, two stiffness-proportional damping models were considered and compared: an initial-stiffness-proportional damping model (ζ_i) and a tangent-stiffness-proportional damping model (ζ_t). Both damping models were calibrated to provide an equivalent viscous damping ratio of 5% in the fundamental mode under elastic conditions. The numerical integration time step, Δ_t, was defined in Equation 12, where Δ_{t_GM} is the sampling interval of the original ground motion record. This criterion ensured adequate resolution of the response across the range of structural periods considered. To allow the SDOF system to shake down into free vibration, zero acceleration was appended to the tail of each ground motion record. The total analysis duration was taken as the maximum of (i) ten times T, (ii) the original record duration, and (iii) twice D.

$$\Delta_t = \min\left(T/20, \Delta_{t\_GM}\right) \tag{12}$$

3.1.1 | Hysteretic Behaviour

Two parameters were used to control hysteretic responses, as marked in Figure 1: the loop dissipation factor, β, and the post-yield stiffness ratio, r. The parameter β governed the extent of energy dissipation within each loading cycle. A value of $\beta = 0$ corresponds to bilinear elastic behaviour, while $\beta = 1$ represents elastic-perfectly plastic behaviour when no post-yield stiffness is present ($r = 0$). The post-yield stiffness ratio r defined the slope of the force-displacement relationship after yielding relative to the initial elastic stiffness. In this study, β was varied from 0.1 to 1.0 in increments of 0.1, and r was varied independently from 0 to 0.9 in increments of 0.1.

3.1.2 | Selection of Structural Period Values

Fundamental periods in this study ranged from 0.2 s to 3.5 s. This period range corresponds to period-to-duration ratios, T/D,

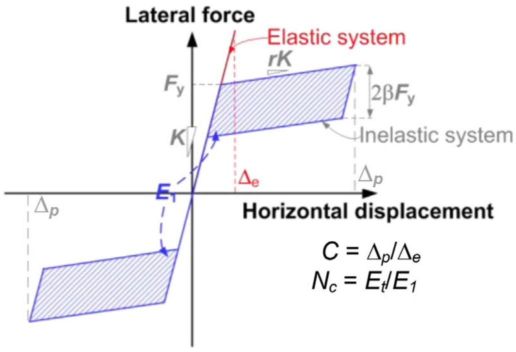

FIGURE 1 | Flag-shaped hysteresis curve illustrating the definition of key parameters.

between 0.014 and 0.25 based on the average significant duration of 14 s. Nonlinear analyses were conducted for 34 uniformly spaced values of T/D spanning the range of interest. For each value of T/D, the corresponding T was determined individually for each ground motion record using its significant duration. For comparison purposes, an additional reference set of analyses was carried out without duration normalization. In this case, structural response was evaluated directly as a function of the fundamental period T, using 34 values uniformly distributed in the period range of interest. This reference set provided a benchmark for assessing the effectiveness of duration normalization in capturing structure responses.

3.1.3 | Response Measures

Two response measures were extracted from each nonlinear analysis. For each specified combination of R, β, r, and T/D (or structural period, T), the two horizontal components of each of the 22 ground-motion record pairs were treated as independent unidirectional excitations, giving 44 response values for each response measure. The geometric mean of these 44 values was calculated as the representative response for that parameter combination. The first was the inelastic displacement ratio defined in Equation 13 and illustrated in Figure 1, where Δ_p is the peak inelastic displacement demand, and Δ_e is the maximum elastic displacement of a SDOF system with the identical mass and the same initial stiffness and subjected to the same ground motion. The second response measure, the number of deformation cycles, N_c, as illustrated in Figure 1, was quantified using an energy-based definition according to MacRae and Kawashima [32], as expressed by Equation 14, where E_t is the total hysteretic energy dissipated over the entire response history, and E_1 is the energy dissipated during a single complete hysteresis loop corresponding to the peak displacement excursion.

$$C = \Delta_p/\Delta_e \tag{13}$$

$$N_c = E_t/E_1 \tag{14}$$

3.2 | Validation With a Full-scale Rocking Structure

To provide an external check of the empirical equations proposed based on the idealized SDOF systems, a validated three-dimensional finite element model (FEM) of a full-scale three-storey steel rocking structure with TOFDs was employed (Zhang et al. [45]), as depicted in Figure 2. The validation of the FEM against shaking-table test results is reported in Zhang et al. [45] and is summarized below to provide context for its use in the present external check. The structure comprised two exterior rocking frames (North and South RFs) and a central gravity frame (GF) in the rocking direction. Energy dissipation was provided by TOFDs and by moment connections in the South–North beams framing into the GF, which partially restrained RF uplift. Frictional grip and grab (GNG) dissipators (Rangwani et al. [12]) were used. Each dissipator consists of a friction connection and a ratchet in which a toothed rack will engage in tension but slides freely and carries almost no force when in compression. This dissipator does not buckle under the cyclical loading due to the absence of large compressive loads, but cumulative tensile deformations of the friction connections occur as a result of ratcheting. To introduce restraint asymmetry, the South–North beam to GF joints used two frictional connection types with comparable strength but distinct hysteretic behaviour: asymmetric friction connections (AFCs) developed by Clifton [46] on the north side and resilient slip friction joints (RSFJs) described by Hashemi et al. [47] on the south side. For the AFCs, the computed moment strengths at sliding initiation were 43, 43 and 29 kNm at Levels 1, 2 and 3, respectively, increasing to 48 kNm (Levels 1/2) and 35 kNm (Level 3) at 3.5% rotation due to prying effects; for the RSFJs, the moment provided by each of the joints at sliding initiation was 36 kNm, and the total moment at 3.5% rotation was 9% lower than that of the AFCs.

The FEM was built in OpenSees and was previously validated against the measured shaking-table responses at the maximum test intensity using the same input record as that used in the shaking table tests, i.e., El Centro 1940 NS (Ulrich [48]). Beams, columns and braces—which remained elastic during the tests—were modelled using elastic beam-column elements with P-Delta geometric transformation, while composite slabs were represented using elastic shell elements. RF base uplifts and both column–foundation and gusset plate - shear key contacts were modelled using compression-only contact elements, as depicted in Figures 2b and 2c, with horizontal sliding at the column bases and gusset out-of-plane motion restrained. These contact elements were represented by two-node link elements assigned a compression-only material model and were excluded from Rayleigh damping contributions. TOFDs were modelled using two-node link elements with the *GNG* material model. The South–North beam-to-GF moment connections were represented using rotational springs, with a *SelfCentring* material assigned to the RSFJ connections and a *MultiLinear* material used for the AFC connections. Tangent-stiffness-proportional Rayleigh damping was adopted and calibrated to 5% critical damping in the first and third translational modes in the rocking direction.

Cyclic push-pull analyses were first conducted, using a first-mode deformation pattern, on two symmetric configurations—RSFJ connections on both sides of the GF and AFC connections on both sides of the GF—to characterize their hysteretic responses and to extract the parameter values required for response prediction. The cyclic push-pull responses used to determine the loop dissipation factor, β, and the post-yield stiffness ratio, r, are presented later in Section 4.8 and Figure 18. The earthquake response was then

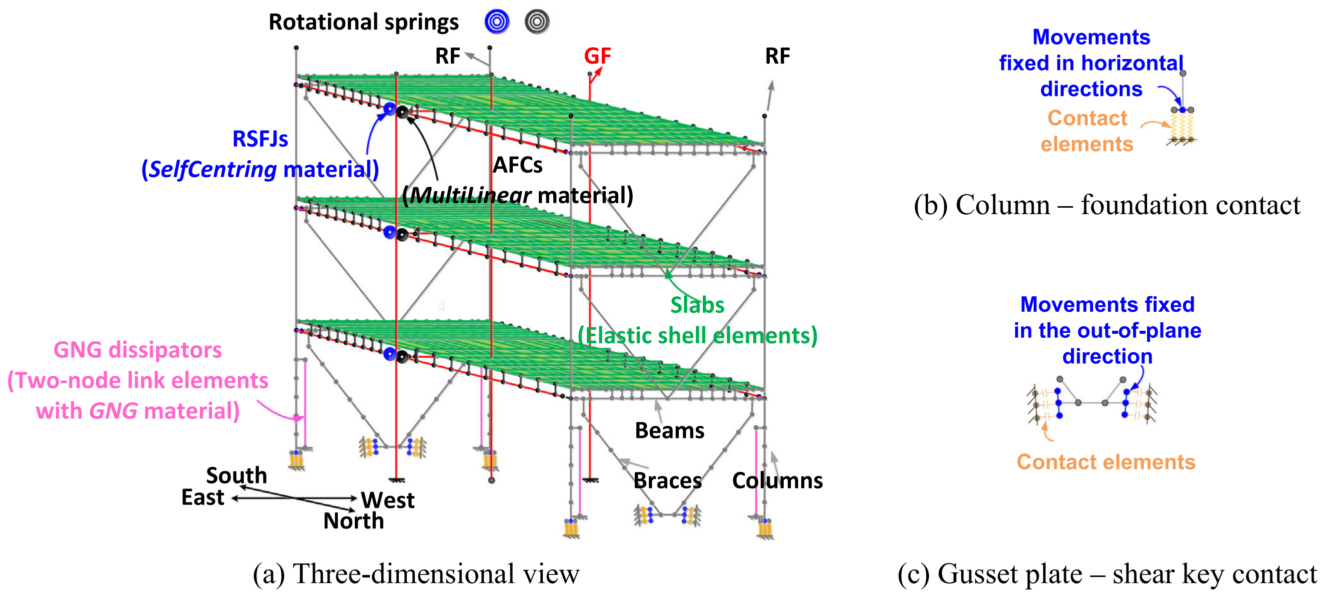

FIGURE 2 | Finite element model of a full-scale three-storey steel rocking structure tested experimentally.

assessed through nonlinear time-history analyses. Whereas the experiments used a single record, the numerical study expanded the input suite using the FEMA P695 far-field records, applied as uniaxial base excitation in the rocking (East-West) direction. Each record was scaled at the fundamental period of the full-scale structure to represent strength-reduction levels R = 2, 4, 6 and 8. For each analysis, the peak roof displacement and the cumulative sliding deformation of the friction connections in TOFDs were extracted for both the North and South RFs. The cumulative sliding deformation was obtained from the column-base uplift time history by summing the positive uplift excursions over the earthquake shaking duration, with the pre-sliding deformation of the GNG dissipator removed cycle-by-cycle, including both deformations arising from elastic stretch and ratchet gap closure. The resulting peak roof displacement and cumulative sliding deformation from the three-dimensional FEM were then compared with those obtained from the SDOF systems with the same β, R, r, and T as the full-scale rocking structure considering height effects, and those predicted by the empirical equations proposed in this study using the nonlinear time-history database generated from SDOF systems as described in Section 3.1. For the SDOF models, the cumulative sliding deformation cannot be extracted directly in the same manner as that for the FEM. It was therefore approximated as the product of the peak uplift displacement and the number of deformation cycles. The peak uplift was inferred from the peak roof displacement using a rigid-body rocking assumption (Zhang et al. [45]).

4 | Behaviour

4.1 | Comparison With Existing Initial-Stiffness-Based Methods

Figure 3 shows a comparison between the mean values of inelastic displacement ratios obtained using SDOF systems with the post-yield stiffness ratio of zero (i.e. r = 0) and initial-stiffness-proportional damping and those calculated with existing initial-stiffness-based methods. NZS 1170.5 [10] generally underestimated the inelastic displacement ratios for low loop dissipation factor values β for R = 4, 6 and 8. The degree of underestimation depended on both the strength-reduction factor R and the period value T. For $R = 2$ and $\beta = 0.1$, the displacement ratio predicted by NZS 1170.5 [10] at the period of 0.2 s was 9.8% higher than the mean numerical result. However, for R = 4, the mean displacement ratio was underestimated by 32% at the same period. More pronounced discrepancies were observed for higher strength-reduction levels, with underestimations of 44% for $R = 6$ and 50% for $R = 8$. The displacement amplification factors in NZS 1170.5 [10] were implicitly calibrated for conventional yielding behaviour with fuller hysteresis loops. As a result, the reduced hysteretic dissipation associated with flag-shaped response was not fully captured, leading to underestimation in the short-period range for the lower β. Compared with NZS 1170.5 [10], SCNZ [11] introduced a constant amplification factor of 1.3 to account for the effect of pinched hysteretic behaviour. However, underprediction of displacements still remained, particularly in the short-period range and for structural systems with lower β and higher R. For $\beta = 0.1$ at $T = 0.2$ s, the underprediction for $R = 4$, 6 and 8 decreased from 32%, 44%, and 50% to 13%, 27%, and 50%, respectively. Miranda [9], which was originally developed for elastic-perfectly plastic behaviour (β = 1), also showed discrepancies for lower β values. For R = 2 and 4, the numerical displacement ratios for β = 1 were consistent with those obtained by the equation but became generally larger as β decreased. For a period of 0.2 s at β of 0.1, the underprediction reached 40% for R = 2 and 34% for R = 4. For R = 6 and 8, the equation continued to underestimate the response in the long-period range for low β values but overestimated the displacement ratios in the short-period range. The overprediction ratios at T of 0.2 s and β of 0.1 were 65% and 228% for R = 6 and 8, respectively. This may be because the equation provided by Miranda [9] was formulated in terms of the displacement ductility factor μ_M and was calibrated over the range $1 \le \mu_M \le 6$. In the present study, the equation was transformed into an R-based relation using $\mu_M = C\mu R$. As a result, for R = 6 and 8, the implied μ_M values exceeded 6 over part of

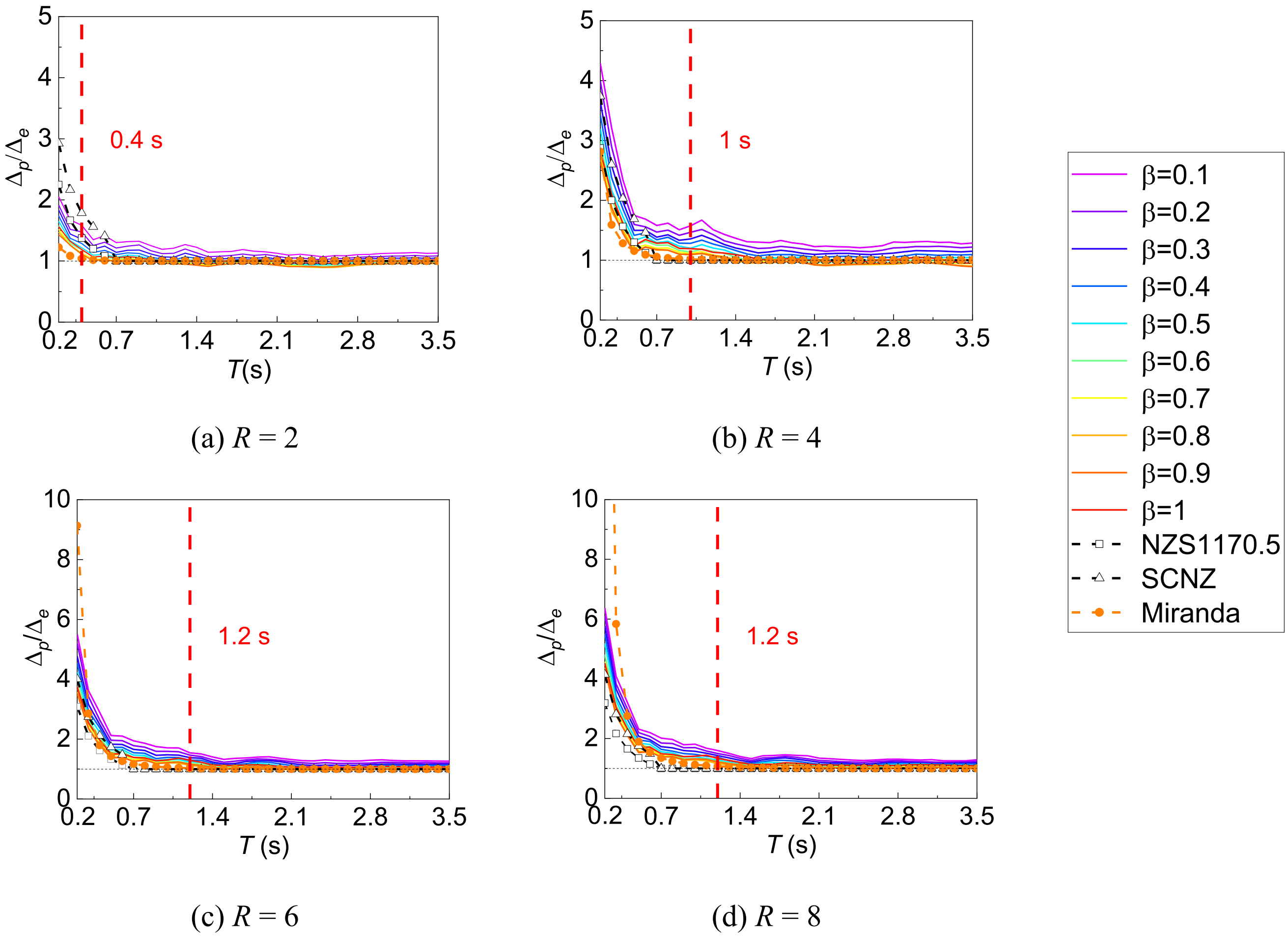

FIGURE 3 | Mean inelastic displacement ratio Δ_p/Δ_e for varying values of β ($r = 0$, $\zeta_i = 5\%$).

the short period range, which lies outside the calibration range considered in Miranda [9].

The transition point was defined as the period beyond which the displacement ratio deviated from its long-period plateau value (at $T = 3.5$ s) by < 0.2. This point was identified for each β and R, and the resulting transition periods were then averaged for each R. Figure 3 indicates that the resulting transition period increased from $R = 2$ to $R = 6$ and remained approximately constant for larger R values, reflecting a saturation of the R-related effect. For the cases investigated, the transition period was approximately $T_s = 0.4$ s for $R = 2$, increasing to $T_s = 1$ s for $R = 4$, and $T_s = 1.2$ s for $R = 6$ and 8. This observed increase in the transition period with increasing R was consistent with the findings of Miranda [9].

4.2 | Effect of β

Figure 3 shows that loop dissipation parameters β influenced Δ_p/Δ_e. When β was reduced slightly from unity to $\beta = 0.9$, a modest reduction in displacement ratio was observed. When $T = 0.2$ s and $R = 2$, the mean displacement ratio decreased from 1.6 for $\beta = 1.0$ to 1.4 for $\beta = 0.9$, corresponding to a reduction of 12%. The reductions were 7%, 5% and 4% for $R = 4$, 6, and 8, respectively. These reductions reflected enhanced dynamic stability (MacRae [13], and MacRae and Kawashima [49]) associated

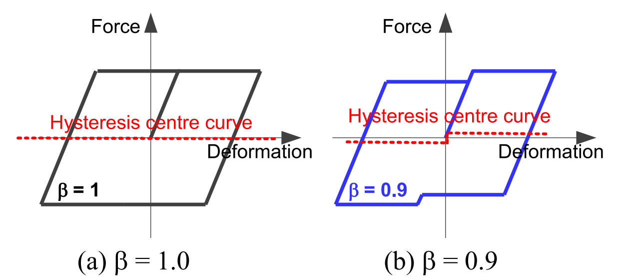

FIGURE 4 | Hysteresis center curve for flag-shaped hysteresis cases.

with the onset of flag-shaped hysteresis responses. As shown in Figure 4, compared with elastic-perfectly plastic behaviour, the hysteresis center curve defined by MacRae [13], and MacRae and Kawashima [49] for the partial self-centring behaviour with $\beta = 0.9$ was in the first or third quadrants, which means the structure was dynamically stable and was less likely to yield away from the initial displacement and deform more in one direction. This phenomenon limited progressive displacement accumulation under repeated loading, even though the overall hysteretic energy dissipation per cycle was slightly reduced as β decreased from 1 to 0.9. As β reduced further below 0.9, the response trend reversed, and the inelastic displacement ratio increased. This increase was observed over the full range of

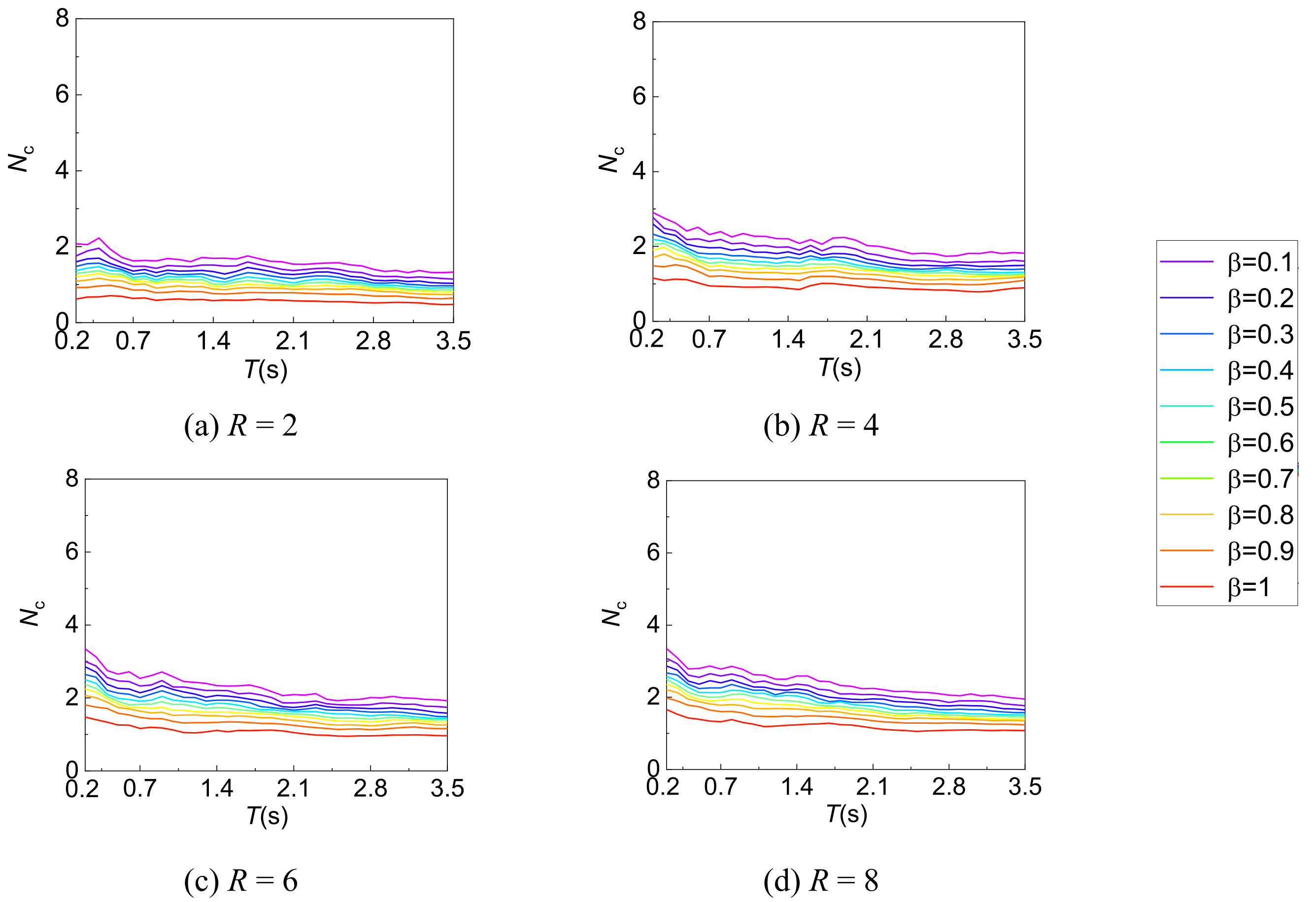

FIGURE 5 | Mean number of cycles of deformation N_c for varying values of β ($r = 0$, $\zeta_i = 5\%$).

structural periods and became more pronounced with increasing strength-reduction factor. For instance, at $T = 0.2$ s, structures with $R = 2$ exhibited an increase in displacement ratios from 1.4 for $\beta = 0.9$ to 2 for $\beta = 0.1$. At the same period, larger relative increases were observed for higher strength-reduction levels, with increases of 1.7, 2, and 2.1 for $R = 4$, 6 and 8, respectively. Expressed as percentages, these increases amounted to 43% for $R = 2$, 65% for $R = 4$, 57% for $R = 6$, and 49% for $R = 8$. This behaviour reflected the progressive reduction in hysteretic energy dissipation as the flag-shaped loop became increasingly slender, allowing larger displacement excursions to develop during earthquake shaking (Farshbaf et al. [16]).

Figure 5 presents the mean N_c with $r = 0$ and varying β. In contrast to the displacement ratio, N_c exhibited a monotonic relationship with β. A representative example at $T = 0.2$ s showed that, for $R = 2$, the mean N_c increased from 0.6 for $\beta = 1.0$ to 0.9 for $\beta = 0.9$, and further to 2.1 for $\beta = 0.1$. The mean N_c increased by 250% as β decreased from 1.0 to 0.1. At the same period, corresponding increases were also observed for higher R, with N_c increasing from 1.2 to 2.9 for $R = 4$, from 1.8 to 3.4 for $R = 6$, and from 1.7 to 3.4 for $R = 8$ as β decreased from 1.0 to 0.1. These changes corresponded to increases of 142%, 89%, and 100% for $R = 4$, 6, and 8, respectively. The monotonic increase in N_c with decreasing β reflected the reduced hysteretic energy dissipation per deformation cycle. As less energy was dissipated during each cycle, the oscillatory motion was sustained for a longer portion of the ground-motion duration, leading to increased cumulative cyclic demands.

4.3 | Effect of *R*

Figures 6 and 7 present mean values of C and N_c, respectively, for SDOF models with $\beta = 0.1$ (representing rocking structures) analyzed using the initial-stiffness-proportional damping model while varying r. Increasing r decreased Δ_p/Δ_e, and as r tended to unity, which implied elastic response, the displacement ratio tended to unity as expected. A representative case at $T = 0.2$ s showed that increasing r from 0 to 0.9 reduced the mean Δ_p/Δ_e by approximately 52% for $R = 2$, with comparable reductions of 74%, 78%, and 83% observed for $R = 4$, 6 and 8, respectively.

The mean number of cycles of deformation, N_c, increased with increasing r, as shown in Figure 7. At a given structural period, elastic structures with r tending to unity exhibited the greatest number of oscillations. Higher values of r indicate a more elastic structural response. Even with a large value of R, when the reduction from the initial elastic stiffness to the post-yield stiffness is small ($r = 0.9$), the hysteresis loop begins to look a bit more like that of an elastic structural system. Consequently, less energy is dissipated, resulting in a larger number of oscillations. For example, at $T = 0.2$ s, the mean value of N_c increased from 2.1 to 2.5 for $R = 2$ as r increased from 0 to 0.9, with

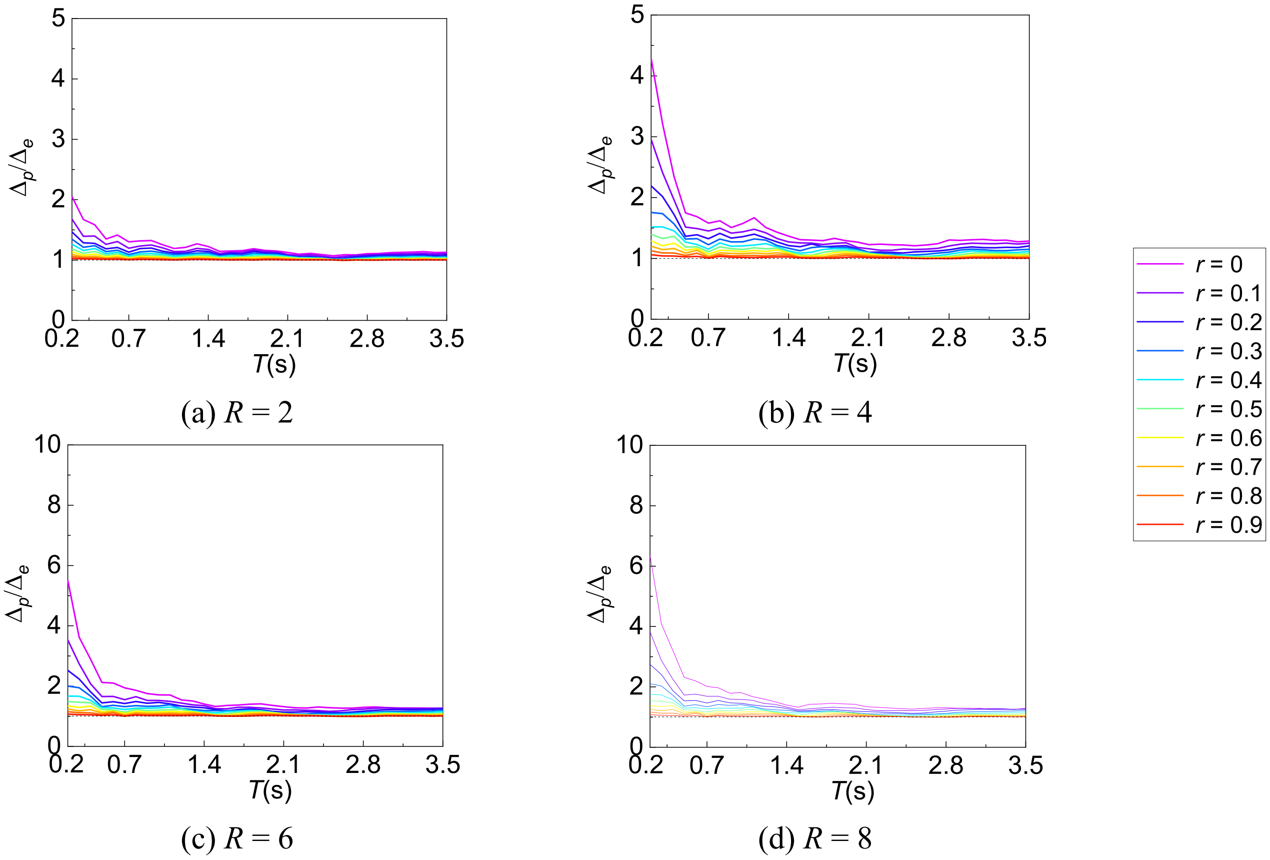

FIGURE 6 | Mean inelastic displacement ratio Δ_p/Δ_e for varying values of r ($\beta = 0.1$, $\zeta_i = 5\%$).

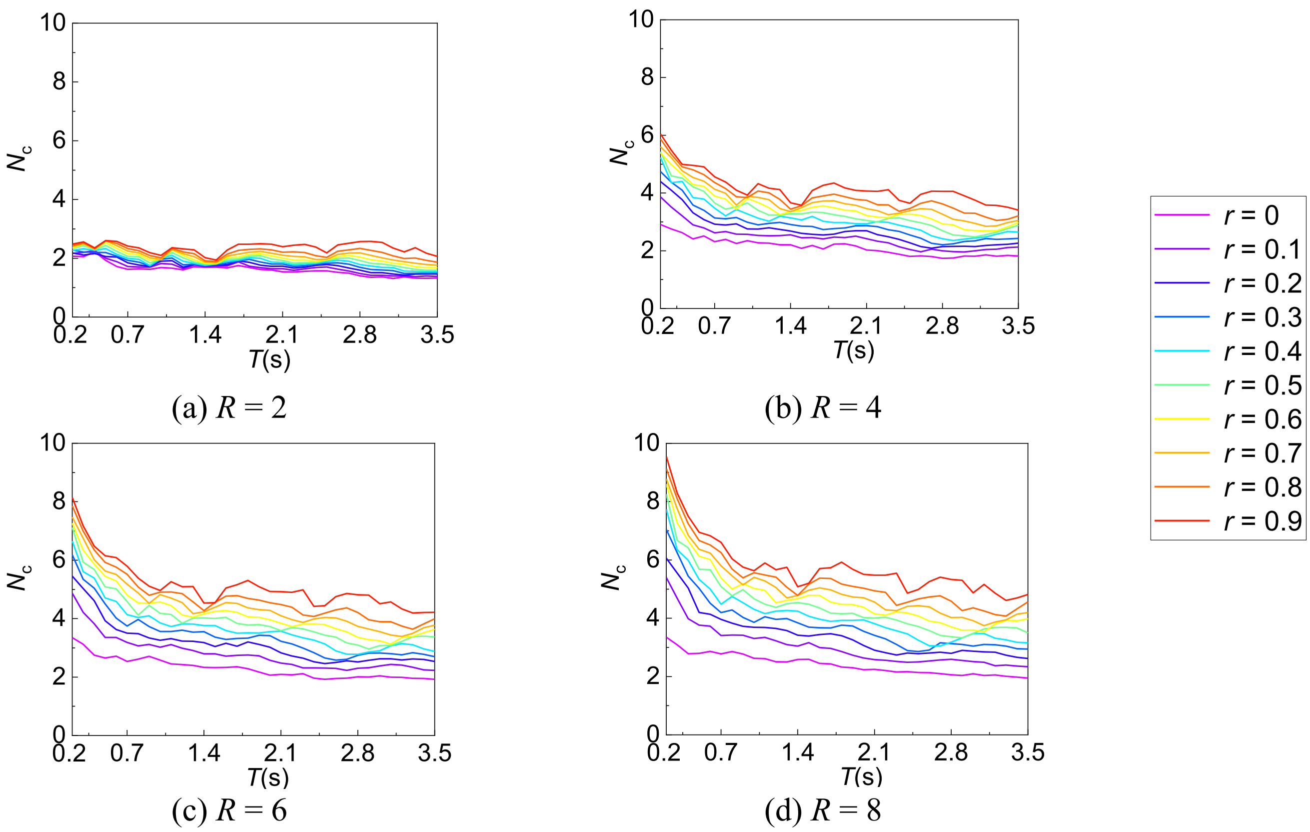

FIGURE 7 | Mean number of cycles of deformation N_c for varying values of r ($\beta = 0.1$, $\zeta_i = 5\%$).

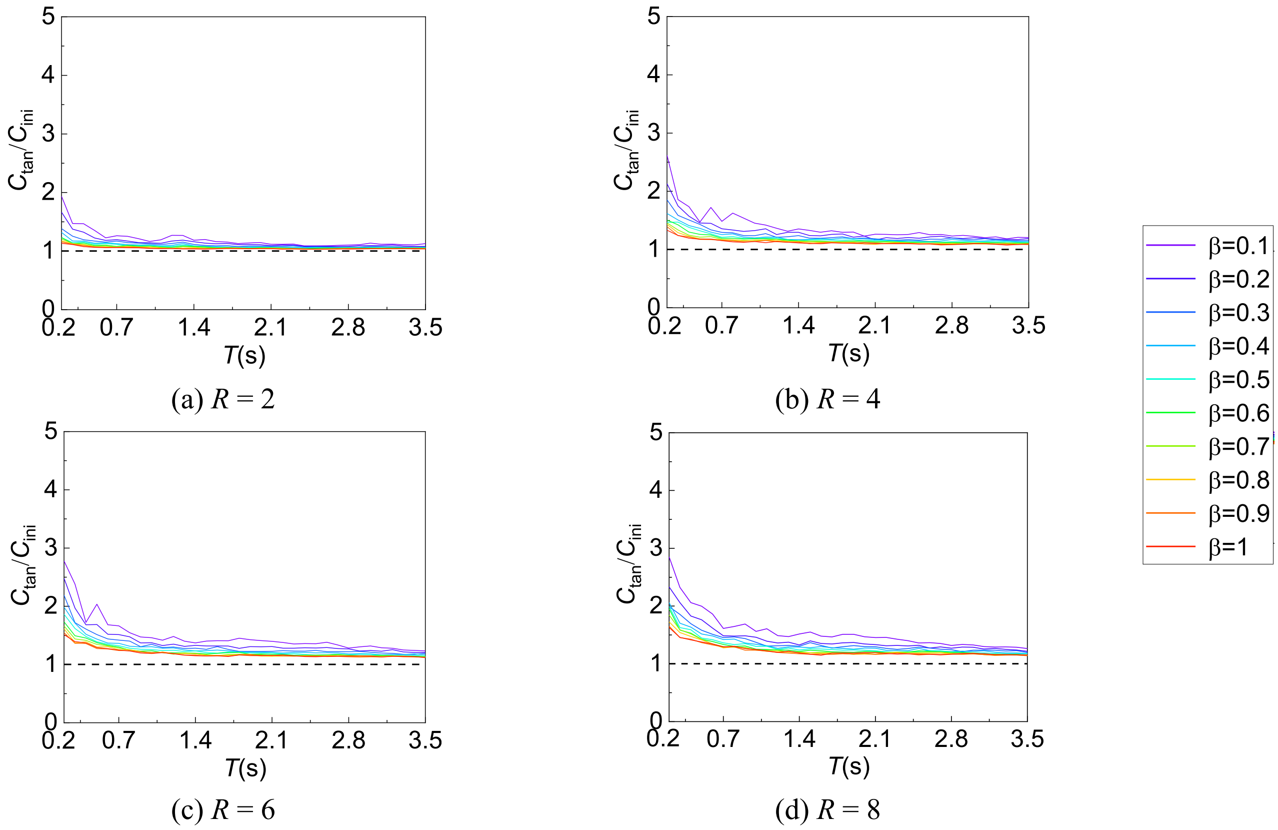

FIGURE 8 | Ratio of mean C obtained using tangent- and initial-stiffness-proportional damping, C_{tan}/C_{ini}, for varying values of β ($r = 0$).

corresponding increases of 3.1, 4.9 and 6.2 observed for $R = 4$, 6 and 8, respectively. This indicated percentage increases of 19%, 107%, 149%, and 182% for $R = 2$, 4, 6, and 8, respectively. While larger values of r were effective in reducing peak displacement demand, they also increased the number of oscillations and may simultaneously increase cumulative deformation demand. This is particularly relevant for rocking systems incorporating TOFDs where there is a limit on the dissipator sliding capacity.

4.4 | Effect of Damping Model

Figures 8 and 9 compare the mean responses obtained using the tangent-stiffness-proportional damping and the initial-stiffness-proportional damping through the ratios C_{tan}/C_{ini} and N_{ctan}/N_{cini}, respectively, where the subscripts "*tan*" and "*ini*" denote the tangent-stiffness and initial-stiffness damping, respectively. The displacement ratio reached its maximum at $r = 0$, whereas the number of cycles generally increased with r. Therefore, $r = 0$ was used to highlight the damping-model effect on displacement demands and $r = 0.3$, a practical upper-bound representative of common structural systems, for numbers of cycles. Compared with initial-stiffness-proportional damping, tangent-stiffness-proportional damping resulted in larger response demands. The influence of the damping model was especially evident for short-period structures and low β values. At $T = 0.2$ s and $\beta = 0.1$, the mean displacement ratio obtained using tangent-stiffness damping increased by 85% for $R = 2$. At the same period and the same β value, the mean displacement ratio increased by 160% for $R = 4$, by 178% for $R = 6$, and by 183% for $R = 8$. Similar trends were observed across the full range of structural periods and loop dissipation factors. Such behaviour was expected because when the stiffness decreased to zero during yielding, the associated damping forces decreased, allowing larger displacement excursions and more sustained oscillatory motions to develop. The tangent-stiffness damping model also led to larger N_c, although the effect was less pronounced than that observed for C. At $T = 0.2$ s and $\beta = 0.1$, the ratio $N_{\mathrm{ctan}}/N_{\mathrm{cini}}$ was 1.12 for $R = 2$, 1.22 for $R = 4$, 1.23 for $R = 6$ and 1.16 for $R = 8$, corresponding to increases of 12%, 22%, 23%, and 16%, respectively. Overall, the use of tangent-stiffness-proportional damping amplified both C and N_c, with the influence being especially evident for short T and low β values.

4.5 | *T/D* versus *T*

Based on the preceding discussions, the empirical equations were developed using responses obtained from the tangent-stiffness-proportional damping, which provided a more conservative representation of both C and N_c. Furthermore, C was best characterized using results obtained for $r = 0$, while N_c was more suitably represented using results obtained for $r = 0.3$, adopted as a practical upper-bound representative of common structural systems. Figure 10 presents the ratio of standard deviations of C obtained using T to that obtained using normalization of T/D (i.e. $\sigma(C_{(T)})/\sigma(C_{(T/D)})$). The earthquake duration D was taken as 14 s, the average duration of the ground motions considered in this study. The comparison was based on the tangent-stiffness-proportional damping with $r = 0$. For short periods, the standard deviation ratio was generally greater than 1.0 for all R, indicating that normalization by T/D produced a smaller dispersion than normalization by T. The maximum ratio value was 2.7 for

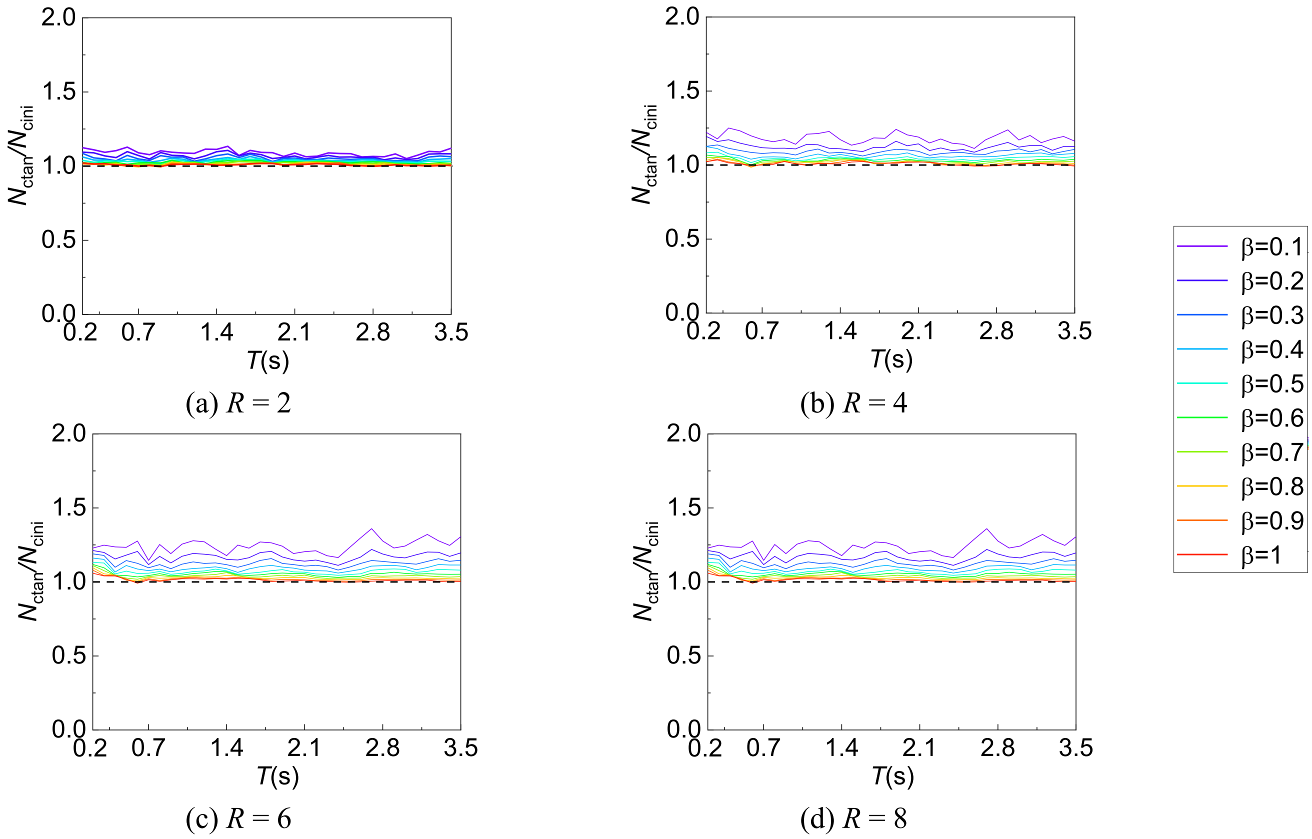

FIGURE 9 | Ratio of mean N_c obtained using tangent- and initial-stiffness-proportional damping, N_{ctan}/N_{cini}, for varying values of β ($r = 0.3$).

$R = 2$, 1.7 for $R = 4$ and 6, and 1.6 for $R = 8$. For longer-period SDOF systems, however, the ratio approached or fell below unity. The minimum ratio was 0.7 for $R = 2$, 4, 6, and 8, indicating that normalization by T led to slightly smaller standard deviations for longer T. Nevertheless, in the long-period region, C approached a nearly constant plateau value, so displacement estimation can be adequately performed using a constant value without explicit dependence on either T or T/D. This trend is attributable to the response being less sensitive to duration for long periods. Figure 11 presents the corresponding standard deviation ratio for N_c (i.e. $\sigma(N_{c(T)})/\sigma(N_{c(T/D)})$) defined in the same manner as the standard deviation ratio for C. Overall, the ratio tended to be greater than 1.0, indicating that normalization by T/D generally produced a smaller dispersion in N_c. However, ratios slightly below 1.0 were still observed in some period intervals. Nevertheless, the dominant trend remains above unity. The ratio varied between 0.8 and 1.6 for $R = 2$, 0.9 and 1.5 for $R = 4$, and 0.9 and 1.8 for $R = 6$ and 8, with the overall trend supporting the use of T/D as the preferred normalizing parameter for N_c. Based on these observations, the empirical equations were formulated using T/D for both C and N_c.

4.6 | Nonlinear Regression Analysis (Displacement Ratio)

The mean displacement ratio C was expressed as a function of R, β, and T/D. For inelastic structural systems ($R > 1$), a piecewise formulation was adopted to account for the distinct response characteristics observed under short and long periods. The measured transition points for the period-to-duration ratio $(T/D)_s$ are 0.04, 0.09, 0.11 and 0.11 for $R = 2$, 4, 6 and 8, respectively. A simple expression for $(T/D)_s$ as a function of R is given in Equation 15.

$$(T/D)_s(R) = 0.11/\left[1 + e^{-1.1(R-2.5)}\right] \tag{15}$$

For large period-to-duration ratios ($T/D > (T/D)_s$), Δ_p/Δ_e was assumed to approach a plateau value C_plat (β, R), given by Equation 16. Based on the regression analysis, the plateau displacement ratio was expressed by Equations 17 and 18. This formulation ensured that $C\_plat(\beta, R) = 1$ for elastic systems ($R = 1$) and increased with R. The comparison between the numerical and predicted plateau displacement ratios is shown in Figure 12.

$$\Delta_p/\Delta_e = C\_plat(\beta, R) \tag{16}$$

$$C\_plat(\beta, R) = 1 + (R-1)^{0.36}\left(0.7\beta^2 - \beta + 0.4\right) \tag{17}$$

$$C\_plat(\beta, R) = 1 + (R-1)^{0.36}(0.04\beta + 0.04) \tag{18}$$

For small period-to-duration ratios ($T/D < (T/D)_s$), the displacement ratio was expressed as Equation 19. This expression ensured continuity of the displacement ratio at $T/D = (T/D)_s$ and allowed the amplification effect to diminish progressively as the period-to-duration ratio increased. The parameters in Equation 19 were calibrated using the non-linear numerical database and took the following final values: $K = 0.43$, $\beta_0 = 0.0092$, $\gamma = -0.32$, $a = 3.2$, $p = 4$, and $b = 1.34$. These parameters were selected to provide a

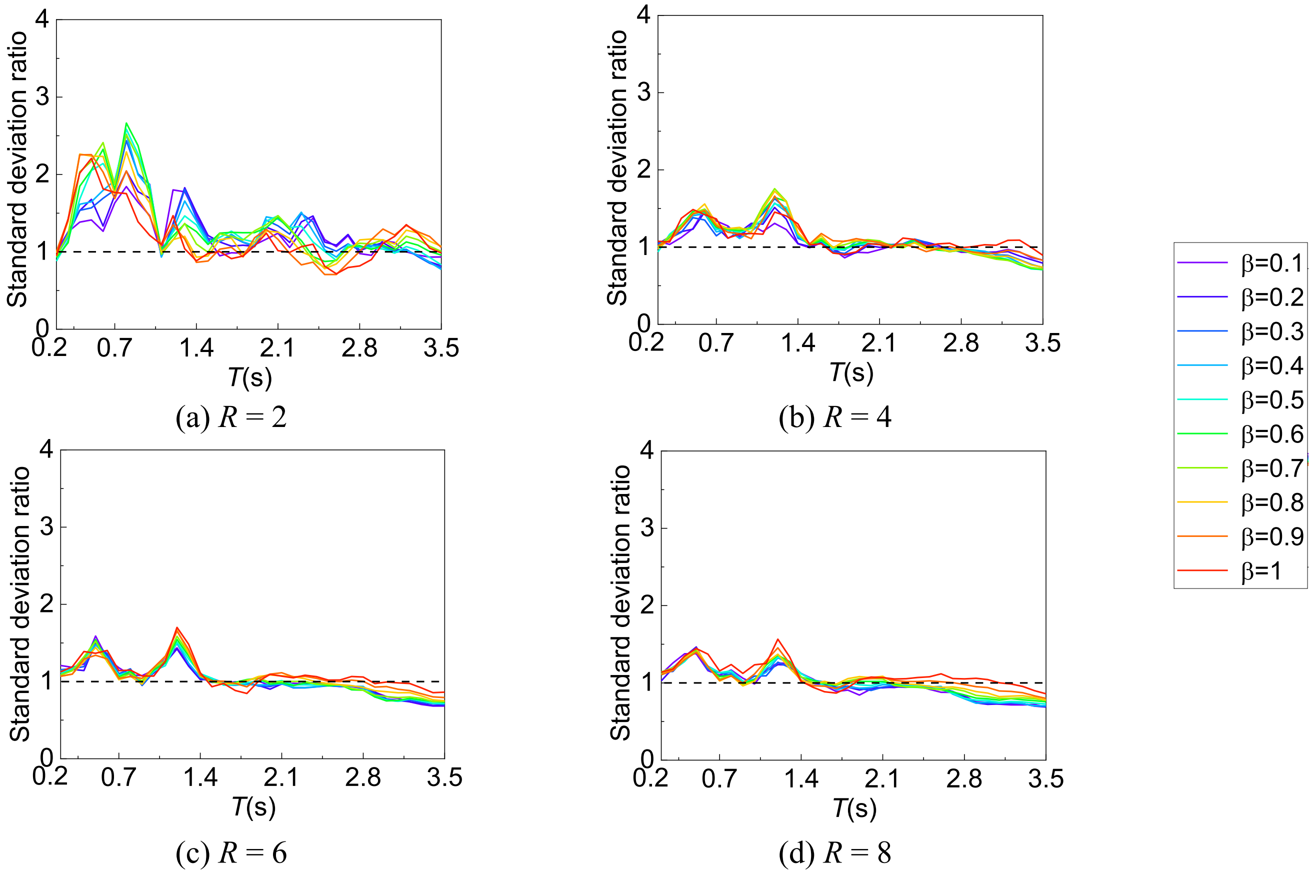

(a) $R = 2$ (b) $R = 4$ (c) $R = 6$ (d) $R = 8$

FIGURE 10 | Ratio of the standard deviation of C when using the structural period T to that obtained using normalization of T/D, $\sigma(C_{(T)})/\sigma(C_{(T/D)})$, for varying values of β ($r = 0$, $\zeta_t = 5\%$).

balanced representation of the displacement response across the full range of R, β, and T/D values, with particular emphasis on improving prediction accuracy for very short-period structures. The roles of these parameters are summarized below.

to-duration ratio T/D decreased below the critical value $(T/D)_s$. Larger values of b resulted in stronger amplification for extremely low period-to-duration ratios.

$$C\left(\beta, R, T/D\right) = C\_plat\left(\beta, R\right)\left\{1 + K(\beta+\beta_0)^{\gamma}\left(1 - \mathrm{e}^{-a(R-1)}\right)^{p}\left[\left(\frac{(T/D)_s\,(R)}{T/D}\right)^{b} - 1\right]\right\} \qquad T/D \le (T/D)_s \tag{19}$$

The constant β_0 of 0.0092 was introduced to prevent singular behaviour as β approached zero. Physically, this ensured that the predicted displacement ratio remained finite for structural systems with very small hysteretic energy dissipation. The exponent γ governed the influence of the hysteretic parameter β on the short-period amplification. A negative value indicated that structural systems with smaller β (i.e., more pronounced pinching or reduced energy dissipation) experienced greater amplification in the peak roof displacement. The final values of a and p were selected as 3.2 and 4, respectively. They governed the sensitivity of the short-period amplification to R. They appeared in the term $[1 - \mathrm{e}^{-a(R-1)}]^p$, which ensured that the amplification effect increased with increasing R but asymptotically approached a saturation level for large values of R. The exponent b controlled the rate at which the displacement ratio increased as the period-

As seen in Figure 13, the final displacement-ratio prediction model (Equation 19) demonstrated good agreement with the nonlinear numerical dataset. As shown in Figure 14, the overall coefficient of determination R^2 was 0.89.

4.7 | Nonlinear Regression Analysis (Number of Cycles of Deformation)

A two-stage prediction model was also proposed for the mean N_c, as expressed by Equations 20 and 21. The transition point was 0.15. Within the range of $0.15 \le T/D \le 0.25$, the difference between the maximum and minimum N_c remained ≤ 0.4.

$$N_c\left(\beta, R, T/D\right) = N_{c\_plat}\left(\beta, R\right) \qquad T/D > 0.15 \tag{20}$$

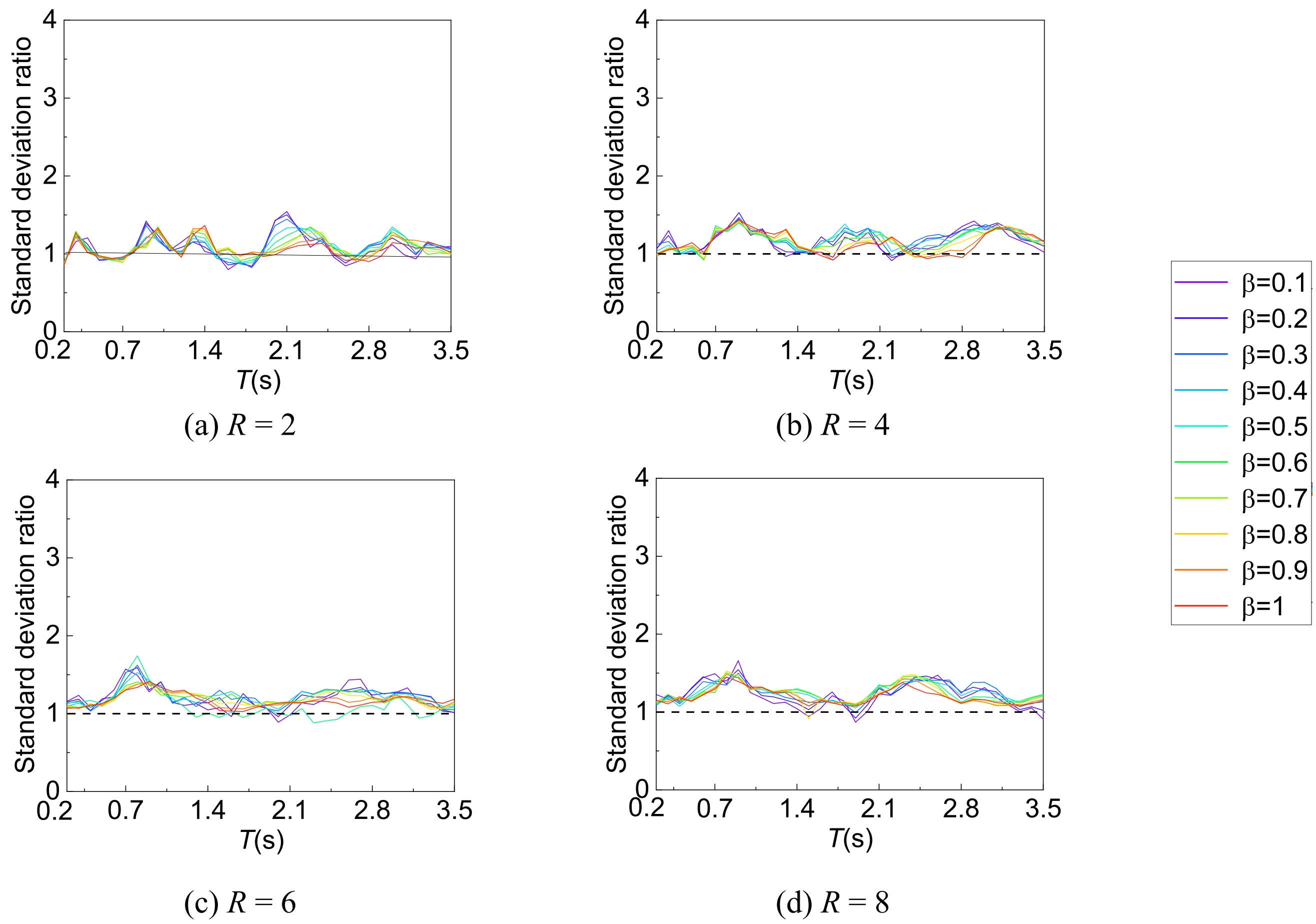

FIGURE 11 | Ratio of the standard deviation of N_c when using T to that obtained using normalization of T/D, $\sigma(N_{c(T)})/\sigma(N_{c(T/D)})$, for varying values of β ($r = 0.3$, $\zeta_t = 5\%$).

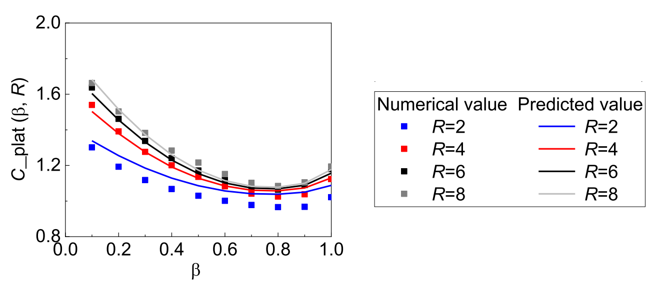

FIGURE 12 | Numerical and predicted plateau displacement ratios ($\zeta_t = 5\%$).

$$N_c(\beta, R, T/D) = N_{c\_plat}(\beta, R)\,[1 + \theta(R)\,\eta(T/D)] \qquad T/D \le 0.15 \tag{21}$$

For each combination of R and β, the plateau value N_{c_plat} (β, R) was defined as the mean N_c within the defined plateau region. The plateau response was represented by Equation 22. The first term governed the residual plateau level for $\beta = 1$, while the second term captured the hysteresis loop effect, which became increasingly significant as β decreased. The equation was determined through least-squares fitting to the plateau values, with iterative refinement to ensure monotonic dependence on β and appropriate scaling with R. The prediction accuracy was quantitatively evaluated by comparing the predicted and numerical plateau values. As indicated in Figure 15, the resulting coefficient of determination R^2 was 0.96.

$$N_{c\_plat}(\beta, R) = 0.7231R^{0.5469} + 0.8002R^{0.4408}(1-\beta)^{1.8883} \tag{22}$$

For $T/D \le 0.15$, the numerical results indicated a monotonic amplification above the plateau. To accurately capture the response at extremely small period-to-duration ratios (T/D = 0.014), a normalized duration variable was introduced, as expressed by Equation 23. This normalization ensured that the short-period modification reached its maximum at $T/D = 0.014$ and decayed smoothly to zero as T/D approached 0.15. Through the normalization procedure, the normalized duration function satisfied $\eta\,(T/D = 0.014) = 1$. Once the response at $T/D = 0.014$ was fixed and the modification term was required to vanish at $T/D =$ 0.15, $\eta\,(T/D)$ served a single role: it controlled the shape of the decay of the short-period amplification within the intermediate range $0.014 < T/D < 0.15$. Consequently, $\eta\,(T/D)$ determined how rapidly the amplification transitions from its maximum value at very short period-to-duration ratios to the plateau response, without influencing the calibrated response at $T/D = 0.014$.

$$\eta\,(T/D) = [(0.15 - T/D)/(0.15 - 0.014)]^{2.2062} \tag{23}$$

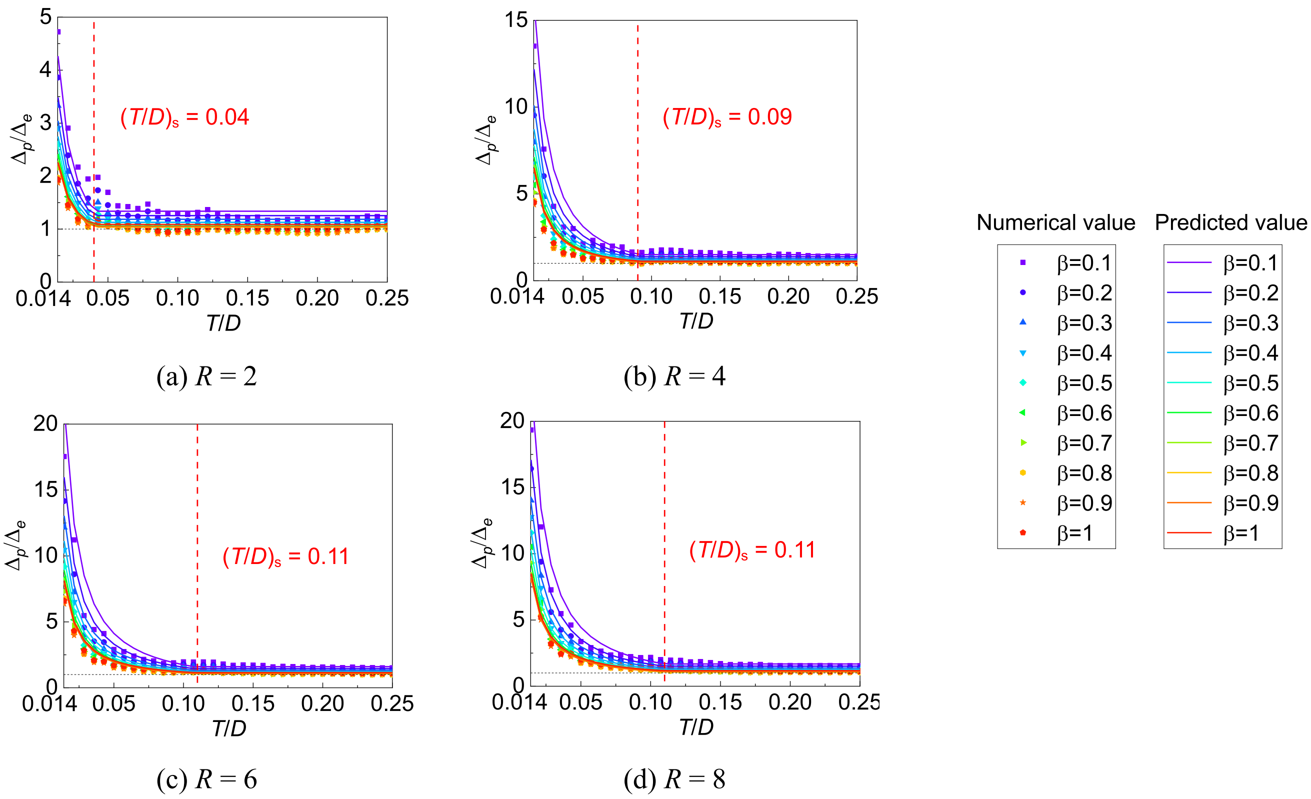

FIGURE 13 | Numerical and predicted mean Δ_p/Δ_e ($\zeta_t = 5\%$).

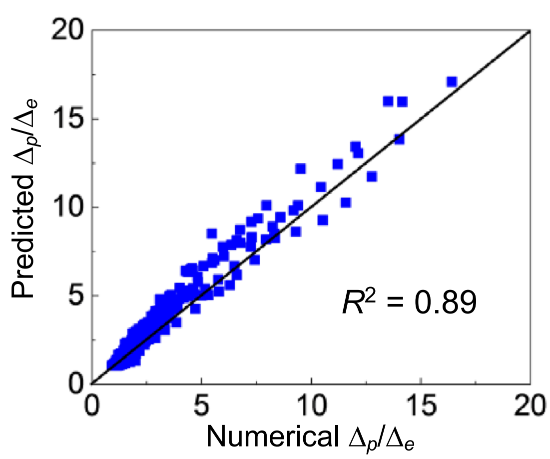

FIGURE 14 | Prediction accuracy (Δ_p/Δ_e) ($\zeta_t = 5\%$).

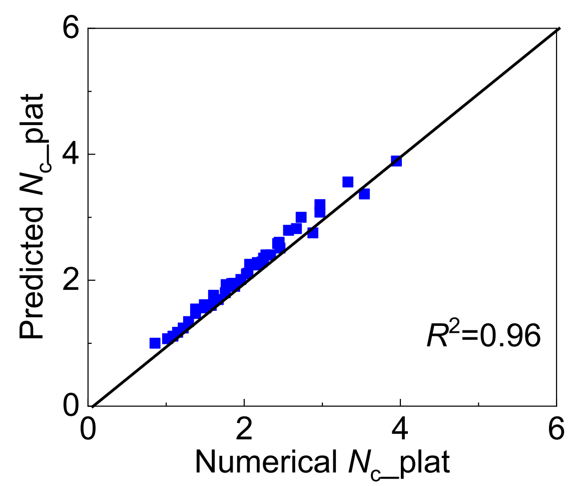

FIGURE 15 | Numerical and predicted plateau N_c ($\zeta_t = 5\%$).

The short-period amplification at T/D = 0.014 was entirely governed by the amplitude function $\theta\,(R)$. Because the dominant requirement was to minimize prediction errors at T/D = 0.014 across all β values, $\theta\,(R)$ was calibrated using the numerical results at $T/D = 0.014$. For each R, a single θ was obtained by least-squares minimization over all β at this period-to-duration ratio, minimizing the variable expressed by Equation 24, where $N_{c}\_plat\ (\beta,\ R)$ denotes the plateau prediction obtained from Equation 22, and $N_{c}\_num\ (T/D = 0.014)$ represents the corresponding numerical value. This calibration procedure ensured that, at T/D = 0.014, the overall prediction error was minimized for all β levels, rather than being tuned to a specific β value.

$$\sum_{-} \beta \left\{ N_{c\_plat}(\beta, R)\left[1 + \theta\eta\,(T/D)\right] - N_{c\_num}\,(T/D = 0.014) \right\}^2 \tag{24}$$

The resulting discrete θ values (one for each R) were subsequently represented by a smooth saturating function to maintain a unified formulation, as indicated by Equation 25 with calibrated parameters $\theta\,(2) = 0.31$, $\theta\,(8) = 1.36$, and $d = 0.62$.

$$\theta\,(R) = \theta\,(2) + [\theta\,(8) - \theta\,(2)]\left[1 - \mathrm{e}^{-d(R-2)}\right] \tag{25}$$

Figures 16 and 17 show a comparison between numerical and predicted results. Equations 20 and 21 accurately captured both

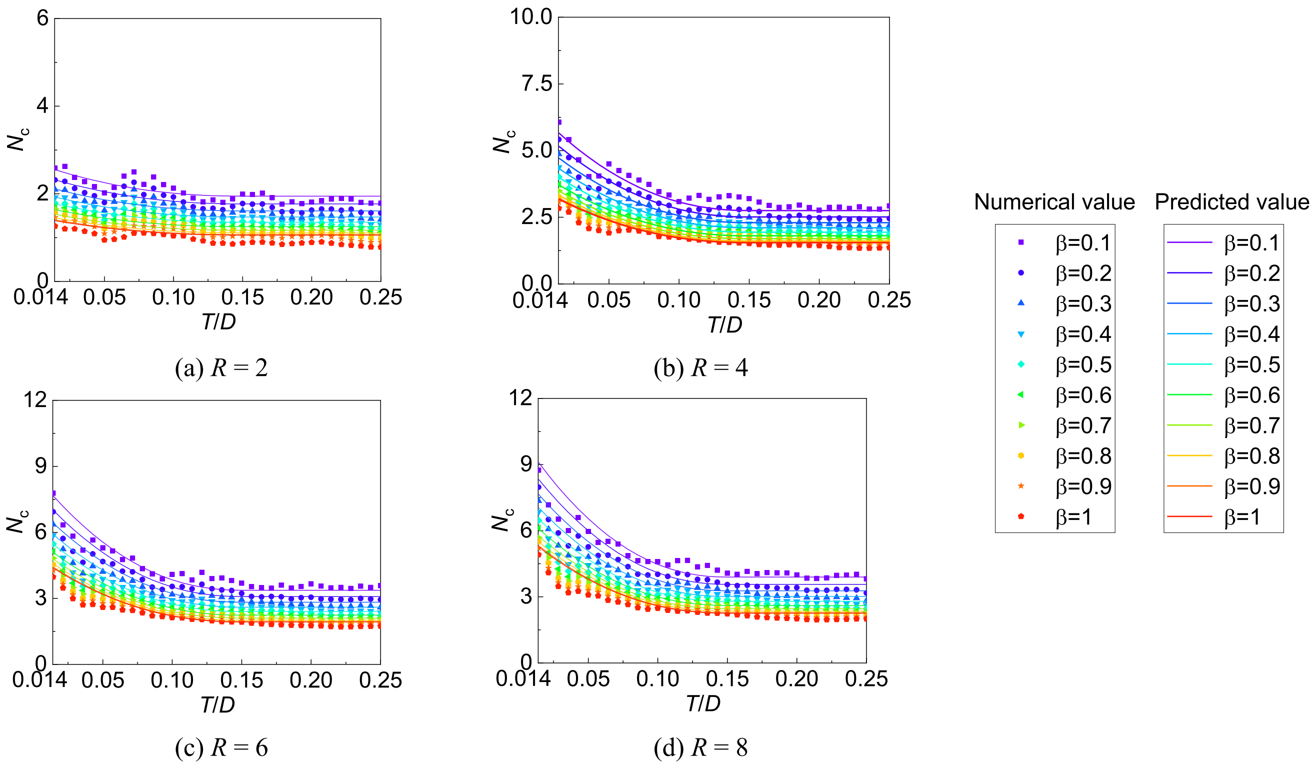

FIGURE 16 | Numerical and predicted mean N_c ($\zeta_t = 5\%$).

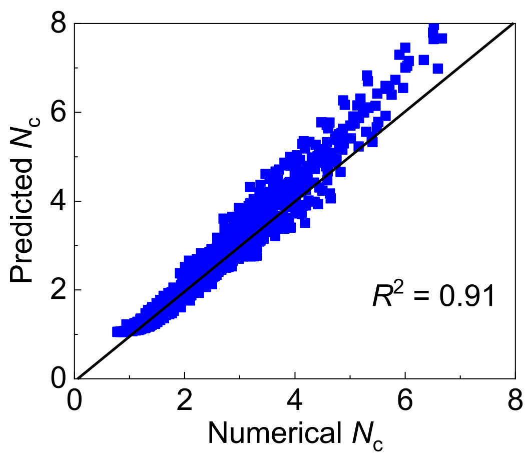

FIGURE 17 | Prediction accuracy.

the plateau behaviour and the amplification trend observed for small T/D. The overall R^2 was 0.91.

4.8 | Validation Against Behaviour of a Full-Scale Rocking Structure

At the maximum shaking intensity applied in the tests (Zhang et al. [45]), the FEM predicted a South-RF peak roof displacement of 71 mm versus 83 mm measured and a North-RF peak roof displacement of 37 mm versus 38 mm measured, while the predicted and measured peak base shears were 654 kN and 594 kN, respectively (10% error). For the RSFJ-symmetric configuration, the idealized flag-shaped loop has a flag-loop dissipation factor of 0.18 and a post-yield stiffness ratio of 0.05, as marked in Figure 18, while for the AFC-symmetric configuration, $\beta = 0.28$ and $r = 0.05$. Both configurations have a fundamental translational period of 0.2 s in the rocking direction. As shown in Figure 19, for $R = 2$, 4, 6 and 8, the mean peak roof displacements of the South RF from the FEM were 30 mm, 116 mm, 212 mm and 314 mm, respectively; the corresponding values for the North RF were 30 mm, 114 mm, 198 mm and 300 mm. Using the SDOF model with $\beta = 0.18$ and $r = 0.05$, the predicted peak roof displacements were 27 mm, 106 mm, 204 mm and 314 mm for $R = 2$, 4, 6 and 8, respectively, while using $\beta = 0.28$ and $r = 0.05$ the corresponding predictions were 25 mm, 95 mm, 178 mm and 292 mm. The mean responses of the rocking structure were greater than those of the SDOF model. The maximum error in the mean peak roof displacements by the SDOF prediction was 17%. The errors of the SDOF prediction for cumulative sliding demands of the TOFDs, as marked in Figure 20, were within 24%. These discrepancies are likely attributable to higher-mode contributions and additional energy dissipation associated with impact that are not captured in SDOF models, together with the simplification of the measured irregular hysteretic response into an idealized flag-shaped representation. The empirical equations proposed in Sections 4.6 and 4.7 generally provided conservative estimates of the peak roof displacement and cumulative sliding demand, as seen in Figures 19 and 20. Across the 22 pairs of earthquake records, the responses predicted by the empirical equations ranged from 0.98 to 3.0 times the corresponding mean FEM responses. The overprediction relative to the maximum FEM response did not exceed 10%. Future work can introduce an r-dependent correction to account for the post-yield stiffness effect, which is expected to reduce the current overprediction.

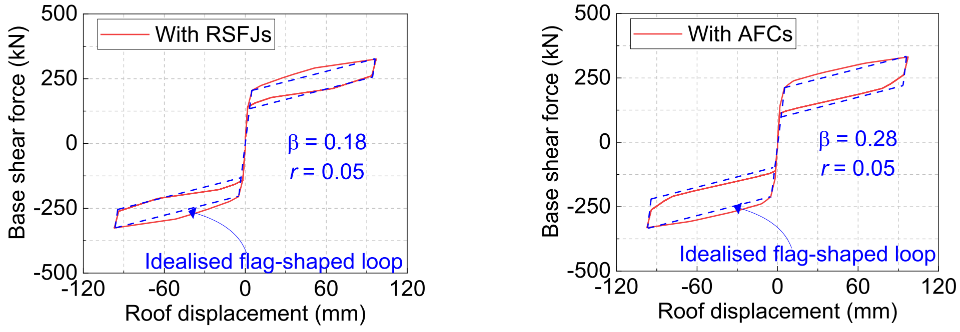

(a) RSFJ-symmetric configuration (b) AFC-symmetric configuration

FIGURE 18 | Cyclic push-pull behaviour under the first-mode deformation pattern.

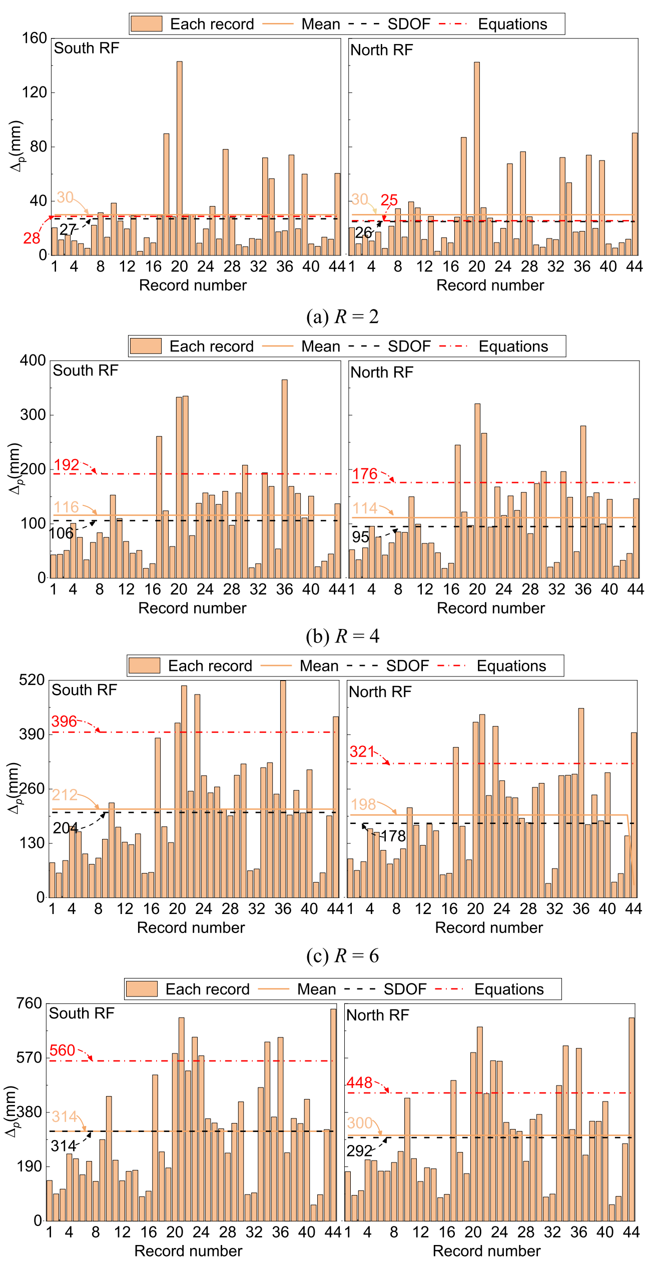

(a) $R = 2$

(b) $R = 4$

(c) $R = 6$

(d) $R = 8$

FIGURE 19 | Peak roof displacements (FEM).

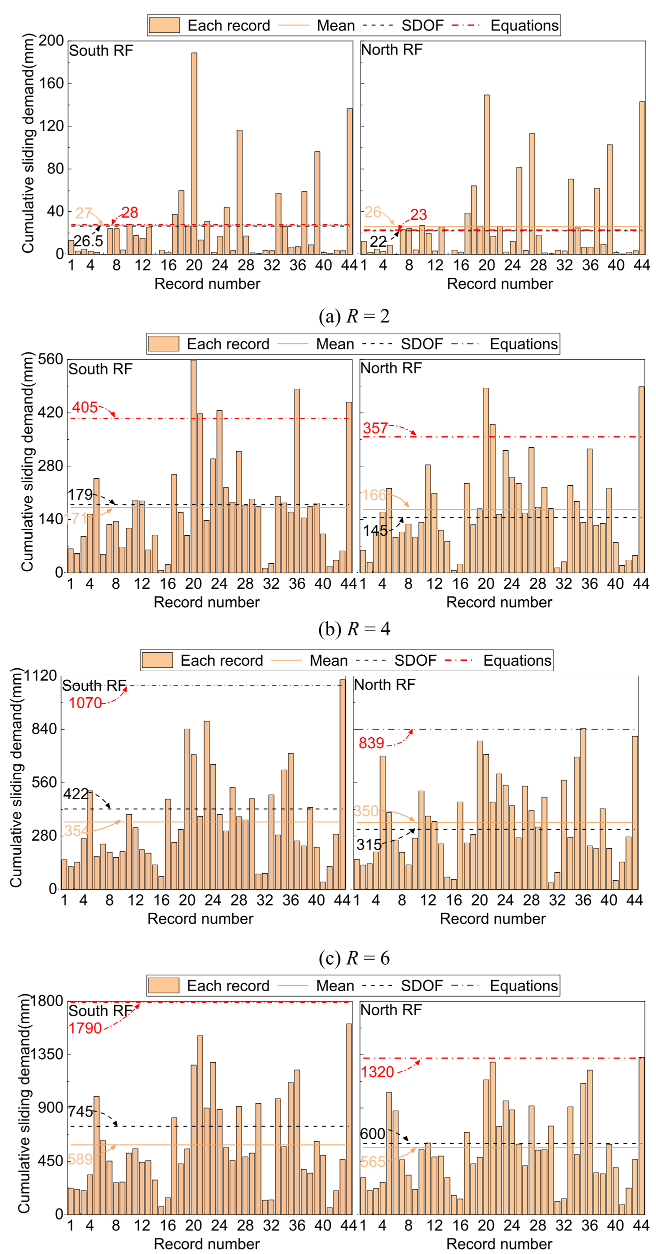

(a) $R = 2$

(b) $R = 4$

(c) $R = 6$

(d) $R = 8$

FIGURE 20 | Cumulative sliding demand (FEM).

5 | Conclusions

This paper investigates the response of structures with a range of flag-shaped hysteretic characteristics focusing on the peak displacement, Δ_p, and the number of cycles of deformation, N_c. A loop dissipation parameter, β, of 0 corresponds to bilinear elastic behaviour, while $\beta = 1$ represents elastic-perfectly plastic behaviour when no post-yield stiffness is present ($r = 0$). It is shown that:

1. The initial-stiffness-based and secant-stiffness-based methods are commonly used to predict displacements. Common secant-stiffness-based methods explicitly consider the hysteresis loop shape, while the initial-stiffness-based methods require a specific correction. Both use empirical relationships and can give good estimations of displacement responses over the range of structural systems for which they are calibrated. However, neither explicitly considers record duration effects together with hysteresis loop shape.
2. When tangent-stiffness proportional damping was considered, rather than the initial stiffness proportional damping, both Δ_p and N_c increased.
3. When the loop dissipation parameter, β, decreased, Δ_p tended to increase. This was particularly significant for structures of short period, T, or short period-to-duration ratio, T/D, as a result of them being subject to more input cycles of loading and being more prone to resonance. Using tangent stiffness proportional damping, the displacements were larger than those calculated according to code equations which were based on initial stiffness proportional damping. Lower r also generally tended to cause larger Δ_p.
4. The number of cycles of deformation, N_c, increased with lower β and higher r.
5. Considering the period-duration ratio T/D, rather than period, T, significantly reduced scatter for both Δ_p and N_c for short-period structures.
6. Unified empirical equations were developed to estimate Δ_p and N_c for different values of β, R, and the period-to-duration ratio, T/D, using tangent-stiffness proportional damping. Overall coefficients of determination $R^2 = 0.89$ and $R^2 = 0.91$ were achieved for Δ_p and N_c, respectively. Conservative equations were proposed to estimate Δ_p assuming $r = 0.0$ and N_c using $r = 0.3$ as a practical upper-bound representative of common structural systems.
7. The geometric mean peak roof displacement of the three-storey rocking structure with tension-only frictional dissipators (TOFDs) subjected to the ground motion suite was similar to that from the SDOF system with the same β, R, $r = 0.05$, and T considering height effects. The differences in peak roof displacements and TOFD cumulative displacements were less than 24%. These differences were likely attributable to (i) impact and re-contact-induced energy dissipation at the structure base that is not represented in the idealized SDOF models, (ii) higher-mode contributions in the full-scale structure, and (iii) the simplification of the measured irregular hysteretic response into an idealized flag-shaped response. The empirical equations, corrected to account for height effects, generally provide conservative estimates of the peak roof displacements and cumulative sliding displacements of the rocking structure, ranging from 0.98 to 3.0 times the corresponding mean responses, because they were developed based on $r = 0$ for Δ_p and 0.3 for N_c.

Author Contributions

Yudi Zhang: conceptualization, methodology, software, formal analysis, data curation, visualization, writing – original draft. **Gregory A. MacRae:** research idea, conceptualization, methodology, supervision, funding acquisition, project administration, and writing – review and editing. **Geoffrey W. Rodgers:** supervision, methodology, and writing – review and editing. **Shahab Ramhormozian:** funding acquisition. **Charles Clifton:** funding acquisition. **Masoumeh Farshbaf:** methodology development, interpretation of duration-related response trends, writing – review and editing.

Acknowledgements

The support from New Zealand Ministry of Business, Innovation and Employment Endeavour Fund for the Research Programme (Sustainable Earthquake Resilient Buildings for a Better Future—PROP-83779-ENDRP-AUT) is greatly appreciated. The authors also gratefully acknowledge the editor for the constructive comments and valuable suggestions that contributed to improving the clarity and quality of this work.

Open access publishing facilitated by University of Canterbury, as part of the Wiley - University of Canterbury agreement via the Council of Australasian University Librarians.

Conflicts of Interest

There is no conflict of interest in the submitted manuscript. I would like to declare on behalf of my co-authors that the work described was original research that has not been published previously and is not under consideration for publication elsewhere, in whole or in part. All the authors listed have approved the manuscript that is enclosed.

Data Availability Statement

The data that support the findings of this study are available from the corresponding author upon reasonable request.

References

1. M. M. Newmark, "Current Trends in the Seismic Analysis and Design of High Rise Structures," in *Proceedings of the Symposium on Earthquake Engineering* (The University of British Columbia, 1965).

2. G. W. Housner, "Limit Design of Structures to Resist Earthquakes," in *Proceedings of the First World Conference on Earthquake Engineering*, Berkeley, California (1956).

3. N. M. Newmark and W. J. Hall, *Earthquake Spectra And Design* (Earthquake Engineering Research Institute, 1982), 103.

4. J. B. Berrill, M. J. N. Priestley, and H. E. Chapman, "Section 2: Design Earthquake Loading and Ductility Demand," *Bulletin of the New Zealand Society for Earthquake Engineering* 13, no. 3 (1980): 232–241.

5. New Zealand National Society for Earthquake Engineering (NZNSEE) Bridge Study Group. "Seismic Design of Bridges, " *Bulletin of the New Zealand Society for Earthquake Engineering* 1980;13, no. 3: 226–309.

6. Standards New Zealand *NZS 4203: General Structural Design and Design Loadings for Buildings* (Standards New Zealand, 1992).

7. FEMA 356. "Prestandard and Commentary for the Seismic Rehabilitation of Buildings," *Federal Emergency Management Agency* 2000, 520.

8. J. K. Song and J. A. Pincheira, "Spectral Displacement Demands of Stiffness- and Strength-Degrading Systems," *Earthquake Spectra* 16, no. 4 (2000): 817–851.

9. E. Miranda, "Inelastic Displacement Ratios for Structures on Firm Sites," *Journal of Structural Engineering* 126, no. 10 (2000): 1150–1159.

10. Standards New Zealand *NZS1170.5: Structural Design Actions Part 5: Earthquake Actions* (Standards New Zealand, 2016).

11. L. Wiebe, G. Sidwell, and S. Gledhill, *SCNZ: Design Guideline for Controlled Rocking Steel Braced Frames*, SCNZ Report 110 (Aurecon New Zealand Limited for SCNZ, 2015).

12. K. Rangwani, G. A. MacRae, and G. W. Rodgers, "Performance of Rocking Frames With Friction Tension-Only Devices," *Bulletin of the New Zealand Society for Earthquake Engineering* 56, no. 2 (2023): 71–90.

13. G. A. MacRae, "P-Δ Effects on Single-Degree-of-Freedom Structures in Earthquakes," *Earthquake Spectra* 10, no. 3 (1994): 539–568.

14. R. Chandramohan, T. Lin, J. W. Baker, and G. G. Deierlein, "Influence of Ground Motion Spectral Shape and Duration on Seismic Collapse Risk," in *10th International Conference on Urban Earthquake Engineering*, Tokyo, Japan (2013).

15. M. Raghunandan and A. B. Liel, "Effect of Ground Motion Duration on Earthquake-Induced Structural Collapse," *Structural Safety* 41 (2013): 119–133.

16. M. Farshbaf, G. A. MacRae, A. S. Moghadam, C. Lee, H. Soleimankhani, and T. L. Chang, "Duration-Period Ratio (DPR) Effect on Estimating Structure Displacements," in *18th World Conference on Earthquake Engineering*, Italy, Milan (2024).

17. E. Erduran and S. K. Kunnath, "Enhanced Displacement Coefficient Method for Degrading Multi-Degree-of-Freedom Systems," *Earthquake Spectra* 26, no. 2 (2010): 311–326.

18. C. Christopoulos, A. Filiatrault, and B. Folz, "Seismic Response of Self-Centring Hysteretic SDOF Systems," *Earthquake Engineering & Structural Dynamics* 31 (2002): 1131–1150.

19. C. Christopoulos, "Frequency Response of Flag-Shaped Single Degree-of-freedom Hysteretic Systems," *Journal of Engineering Mechanics* 130, no. 8 (2004): 894–903.

20. S. Kitayama and M. C. Constantinou, *Development and Evaluation of Procedures for Analysis and Design of Buildings With Fluidic Self-centering Systems*, MCEER-16-0003 (Multidisciplinary Center for Earthquake Engineering Research, State University of New York at Buffalo, 2016).

21. S. Kitayama and M. C. Constantinou, "Seismic Response Analysis of Single-Degree-of-Freedom Yielding Structures With Fluidic Self-Centering Systems," *Engineering Structures* 125 (2016): 266–279.

22. S. Kitayama and M. C. Constantinou, "Design and Analysis of Buildings With Fluidic Self-Centering Systems," *Journal of Structural Engineering* 142, no. 11 (2016): 04016105.

23. P. Gulkan and M. A. Sozen, "Inelastic Responses of Reinforced Concrete Structure to Earthquake Motions," *Journal Proceedings* 71, no. 12 (1974): 604–610.

24. M. J. N. Priestley, G. M. Calvi, and M. J. Kowalsky, *Displacement-based Seismic Design of Structures* (IUSS Press, 2007).

25. C. J. Ceballos and T. Sullivan, "Development of Improved Inelastic Displacement Prediction Equations for the Seismic Design of Hybrid Systems," *Bulletin of the New Zealand Society for Earthquake Engineering* 45, no. 1 (2012): 1–14.

26. T. J. Sullivan, "Guidance on the Use of Equivalent Viscous Damping for Seismic Assessment," in *Proceedings of the 2016 New Zealand Society for Earthquake Engineering Conference*, Christchurch, New Zealand (2016).

27. Y. Zhou, W. Tian, Y. Xiao, M. O. Eberhard, and J. F. Stanton, "An Equivalent Damping Ratio That Accounts for Ground-Motion Spectral Shape for Displacement-Based Design of Flag-Shaped Hysteresis Systems," *Earthquake Spectra* 39, no. 3 (2023): 1779–1805.

28. G. A. MacRae, *ENEQ650: Advanced Earthquake Engineering* (University of Canterbury, 2025).

29. H. Krawinkler and M. Zohrei, "Cumulative Damage in Steel Structures Subjected to Earthquake Ground Motions," *Computers & Structures* 16, no. 1-4 (1983): 531–541.

30. Y. J. Park and A. Ang, "Mechanistic Seismic Damage Model for Reinforced Concrete," *Journal of Structural Engineering* 111, no. 4 (1985): 722–739.

31. G. A. MacRae, *The Seismic Response of Steel Frames (Doctoral dissertation). Civil Engineering* (University of Canterbury, 1989).

32. G. A. MacRae and K. Kawashima, "The Seismic Response of Bilinear Oscillators Using Japanese Earthquake Records," *Journal of Research of the Public Works Research Institute, Ministry of Construction* 30 (1993): 173P.

33. J. Hancock and J. J. Bommer, "The Effective Number of Cycles of Earthquake Ground Motion," *Earthquake Engineering & Structural Dynamics* 34, no. 6 (2005): 637–664.

34. J. Cook, G. W. Rodgers, and G. A. Macrae, "Design, Testing and Simulation of Grip 'N' Grab Ratcheting, Tension-only Devices for Seismic Energy Dissipation Systems (Doctoral dissertation)," *Journal of Earthquake Engineering* 24, no. 2 (2018): 328–349.

35. W. Du, X. Yu, and G. Wang, "Prediction Equations for the Effective Number of Cycles of Ground Motions for Shallow Crustal Earthquakes," *Soil Dynamics and Earthquake Engineering* 125 (2019): 105759.

36. A. Arias, "A Measure of Earthquake Intensity," in *Seismic Design for Nuclear Power Plants*, ed. Hansen RJ (MIT Press, 1970), 438–483.

37. M. D. Trifunac and A. G. Brady, "A Study on the Duration of Strong Earthquake Ground Motion," *Bulletin of the Seismological Society of America* 65, no. 3 (1975): 581–626.

38. J. J. Bommer and A. Martínez-Pereira, "The Effective Duration of Earthquake Strong Motion," *Journal of Earthquake Engineering* 3, no. 2 (1999): 127–172.

39. J. J. Bommer, J. Hancock, and J. E. Alarcón, "Correlations Between Duration and Number of Effective Cycles of Earthquake Ground Motion," *Soil Dynamics and Earthquake Engineering* 26, no. 1 (2006): 1–13.

40. R. Park, "Evaluation of Ductility of Structures and Structural Assemblages From Laboratory Testing," *Bulletin of the New Zealand Society for Earthquake Engineering* 22, no. 3 (1989): 155–166.

41. American Institute of Steel Construction in *ANSI/AISC 341-05: Seismic Provisions for Structural Steel Buildings* (American Institute of Steel Construction, 2005).

42. M. Farshbaf, A. S. Moghadam, G. A. MacRae, C. L. Lee, H. Soleimankhani, and T. L. Chang, "Energy Considerations for Estimating Displacements of Oscillators With Different Hysteresis Shapes," in *NZSEE Conference*, Wellington, New Zealand (2022).

43. Federal Emergency Management Agency *FEMA P695: Quantification of Building Seismic Performance Factors* (Federal Emergency Management Agency, 2009).

44. S. Mazzoni, F. McKenna, and M. H. Scott, *OpenSEES: Open System for Earthquake Engineering Simulation Pacific Earthquake Engineering Research Centre (PEER)* (University of California, 2009).

45. Y. Zhang, G. MacRae, G. Rodgers, et al., "Shaking Table Behaviour of a Full-Scale Three Storey Steel Rocking Structure With Tension-Only Frictional Dissipators," *Earthquake Engineering & Structural Dynamics* 55, no. 9 (2026): 1769–1787.

46. G. C. Clifton, *Semi-Rigid Joints for Moments Resisting Steel Framed Seismic Resisting Systems (Doctoral Dissertation)* (Department of Civil and Environmental Engineering, University of Auckland, 2005).

47. A. Hashemi, P. Zarnani, and P. Quenneville, "Earthquake Resilient Cross Laminated Timber (CLT) Lateral Load Resisting System With Innovative Resilient Slip Friction Joints (RSFJs)," in *SESOC Conference*, Wellington, New Zealand (2017).

48. F. P. Ulrich, "The Imperial Valley Earthquake of 1940," *Bulletin of the Seismological Society of America* 31 (1941): 13–31.

49. G. A. MacRae and K. Kawashima, "Post-Earthquake Residual Displacements of Bilinear Oscillators," *Earthquake Engineering & Structural Dynamics* 26, no. 7 (1997): 701–716.